PTEN loss shapes macrophage dynamics in high grade serous ovarian carcinoma

Sarah Spear[1], Olivia Le Saux[1,2], Hasan B. Mirza[1], Nayana Iyer[1], Katie Tyson[1], Fabio Grundland Freile[1], Josephine B. Walton[3,4], Chloé Woodman[1], Sheba Jarvis[5], Darren P. Ennis[1], Carmen Aguirre Hernandez[1], Yuewei Xu[1], Pavlina Spiliopoulou[1,3], James D. Brenton[6], Ana P. Costa-Pereira[1], David P. Cook[7], Barbara C. Vanderhyden[7], Hector C. Keun[1], Evangelos Triantafyllou[8], James N. Arnold[9] and Iain A. McNeish[1]*

*corresponding author
Email: i.mcneish@imperial.ac.uk
Address: IRDB Building, Hammersmith Hospital, LONDON W12 0NN, UK
Tel: +44 20 7594 2792

[1] Ovarian Cancer Action Research Centre, Department of Surgery & Cancer, Imperial College London; London, United Kingdom.
[2] Centre Léon Bérard, Department of Medical Oncology, Lyon, France
[3] Institute of Cancer Sciences, University of Glasgow, Glasgow, United Kingdom.
[4] Centre for Cancer and Inflammation, Barts Cancer Institute, Queen Mary University of London, London, United Kingdom.
[5] Department of Surgery & Cancer, Imperial College London; London, United Kingdom.
[6] CRUK Cambridge Institute, University of Cambridge, United Kingdom.
[7] Department of Cellular and Molecular Medicine, University of Ottawa, Ottawa, Ontario, Canada
[8] Department of Metabolism, Digestion and Reproduction, Imperial College London; London, United Kingdom.
[9] School of Cancer and Pharmaceutical Sciences, King's College London, London, United Kingdom.

Running title

HMOX1-high macrophages in ovarian high grade serous carcinoma

Conflict of interest statement

The authors declare that they have conflicts of interest to declare

Significance Statement

Macrophages with elevated HMOX1 expression are enriched in *PTEN*-deficient high-grade serous ovarian carcinoma, promote tumor growth, and represent a potential therapeutic target.

Abstract

High-grade serous ovarian carcinoma (HGSC) remains a disease of poor prognosis that is unresponsive to current immune checkpoint inhibitors. Although PI3K pathway alterations, such as *PTEN* loss, are common in HGSC, attempts to target this pathway have been unsuccessful. We hypothesized that aberrant PI3K pathway activation may alter the HGSC immune microenvironment and present a targeting opportunity. Single-cell RNA sequencing identified populations of resident macrophages specific to *Pten*-null omental tumors in murine models, which were confirmed by flow cytometry. These macrophages derived from peritoneal fluid macrophages and had a unique gene expression program, marked by high expression of the enzyme heme oxygenase-1 (HMOX1). Targeting resident peritoneal macrophages prevented the appearance of $HMOX1^{hi}$ macrophages and reduced tumor growth. Furthermore, direct inhibition of HMOX1 extended survival *in vivo*. RNA sequencing identified IL33 in *Pten*-null tumor cells as a likely candidate driver leading to the appearance of $HMOX1^{hi}$ macrophages. Human HGSC tumors also contained $HMOX1^{hi}$ macrophages with a corresponding gene expression program. Moreover, the presence of these macrophages correlated with activated tumoral PI3K/mTOR signaling and poor overall survival in HGSC patients. In contrast, tumors with low numbers of $HMOX1^{hi}$ macrophages were marked by increased adaptive immune response gene expression. These data suggest targeting $HMOX1^{hi}$ macrophages as a potential therapeutic strategy for treating poor prognosis HGSC.

Introduction

High grade serous carcinoma (HGSC), the commonest type of ovarian cancer, remains a disease of poor prognosis, especially for patients whose tumors are classified as having proficient homologous recombination (1). The immune microenvironment has a strong prognostic effect in HGSC (2). The presence of intra-epithelial $CD8^+$ T cells (3) and immunoreactive gene expression signatures (4) both correlate with improved overall survival whilst intra-tumoral Treg are associated with poor survival (5). However, responses to immune checkpoint inhibitors are poor with little correlation between response and either platinum-free interval or tumor cell PD-L1 expression (6). Putative neoantigens can be identified in HGSC (7), but average mutational burden is low (8).

PTEN is a tumor suppressor and negative regulator of the PI3K signaling pathway. Although deleterious single nucleotide variants and deletions in *PTEN* are rare in HGSC (4), inactivation through complex re-arrangements is more frequent (9), and complete (13–59%) or partial (13–55%) PTEN protein loss is common (10,11), suggesting transcriptional dysregulation. Furthermore, genomic alterations in the PI3K/RAS signaling pathway occur in 45% of HGSC (4) and enhanced PI3K pathway signaling is observed in the presence of PTEN protein expression (12). Thus, the PI3K pathway represents an important therapeutic target in HGSC. However, clinical trials of small molecule inhibitors have been largely negative so far (13) and there remains a need to identify effective therapeutic strategies for these tumors.

We hypothesized that loss of PTEN and activated PI3K signaling supports HGSC growth in part through an interaction with the tumor microenvironment. Using murine models, we identified that PTEN loss drives expansion of a resident macrophage population in omental tumors, marked by high expression of the enzyme heme-oxygenase 1 (HMOX1), that likely derives from peritoneal fluid macrophages. We demonstrated that similar $HMOX1^{hi}$ macrophages can be identified in human HGSC samples and are associated with aberrant PI3K pathway activity and poor survival. Finally, we also show that targeting of this population of macrophages may have therapeutic potential in HGSC.

Materials and Methods

Cell culture

Generation of ID8 cells with deletions in *Trp53, Pten* and *Brca2* has been described previously(14,15). ID8 cells were cultured in high-glucose 4.5 g/L DMEM (Life Technologies #21969035) supplemented with 4% heat-inactivated fetal bovine serum (Sigma and Life Technologies), 2mM glutamine (Life Technologies #25030024), ITS (Life Technologies #41400045) (10 µg/mL insulin, 5.5 µg/mL transferrin, and 6.7 ng/mL sodium selenite). HGS2 cells were purchased from Ximbio and were grown as previously described (16) in DMEM:F12 Glutamax (Life Technologies #31331028), 4% FBS, murine epidermal growth factor (20 ng/ml) (Sigma #E4127) and Hydrocortisone (100 ng/ml) (Sigma #H0135), ITS. Early experiments were also performed 100 U/ml penicillin, 100 µg/ml streptomycin, 250 ng/ml Amphotericin B (Life Technologies 15240096) or 100 U/ml penicillin/100 µg/ml streptomycin. All cells were grown in 5% CO_2, 37°C with humidity and used for a maximum of 10 passages. Cells were passaged using 0.1% Trypsin-EDTA (Gibco #15400054). Cells were regularly tested for mycoplasma using the Lonza MycoAlert^{TM} detection kit and were always negative.

In vivo experiments

All *in vivo* work was performed at the Central Biological Services facility, Imperial College London in accordance with the U.K. Animals (Scientific Procedures) Act 1986 under Project Licenses 70/7997, P2FEA2F22 and PA780D61A and following approval by the Imperial College AWERB (Animal Welfare and Ethical Review Body). Female C57BL6/J mice aged 6-7 weeks were purchased from Charles River, U.K. B6.129 (Cg)-Ccr2tm2.1Ifc/J) (*Ccr2*$^{RFP/RFP}$) mice were purchased from JAX (strain #017586). Both aged-matched C57BL6/J mice and in-house bred WT mice were used as controls for *Ccr2*$^{RFP/RFP}$ mice. Female 494C57BL/6L Y5.1 (CD45.1) mice aged 6-7 weeks were purchased from Charles River (strain #494) and used at 17 weeks. HO-1-Luciferace-eGFP- knock-in mouse (*Hmox1*^{GFP}) mice were generated as previously (17). All mice were acclimatized for at least 1 week prior to experiments. Mice were injected intraperitoneally with 1x10^6 ID8 cells in 200 µl PBS or 10x10^6 HGS2 cells in 200–300 µl PBS. Mice were monitored regularly and killed upon reaching moderate severity limit as permitted by the Project License limits, which included weight loss, reduced movement, hunching, jaundice and abdominal swelling.

In vivo treatments

Sn (IV) Mesoporphyrin IX dichloride (SnMP) (Inochem #SNM321) was dissolved in 0.1M sterile NaOH and 0.5M $NaHCO_3$ and injected I.P. at 25 µmol/kg. For fixed time point and flow cytometry analysis, mice were injected with ID8 cells on day 0 and SnMP was administered once daily (o.d.) from day 14 – 28, and mice were harvested on day 28. For the survival experiment, mice were injected with ID8 cells on day 0 and SnMP was administered o.d. from day 14 – 28, and mice were harvested upon when reaching humane endpoints. Mice with abdominal swelling but not yet at humane endpoint stopped receiving treatments (usually 1-3 days) before being culled to avoid bleeding.

RNA extraction and cDNA synthesis

Cell medium was removed from 24-well plates and 350 µl RLT buffer added and frozen at -80°C. Plates were thawed on ice and 70% ethanol was added, gently mixed, and transferred into a RNeasy Micro Kit column (Qiagen #74104). RNA extraction was performed as per manufacturer's instructions, including DNase step (Qiagen #79254). RNA was eluted in 30 µl nuclease free H_2O and concentrated estimated using a Nanodrop. 2 µg of RNA was input into each 20 µl cDNA reaction using the High-Capacity cDNA Reverse Transcription Kit (Applied Biosystems #4368814) under cycling conditions 25°C 10 mins, 37°C 120 mins, 85°C 5 mins. The cDNA was diluted in 140 µl nuclease free H_2O. qRT-PCR reaction was setup using 9 µl cDNA, 1 µl primer and 10 µl TaqMan Universal Master Mix II no UNG (Thermofisher #4440040). TaqMan primer probes were purchased from Thermofisher, *Rpl34* (Mm01321800_m1), *Ccl2* (Mm00441242_m1), *Ccl7* (Mm00443113_m1), *Csf1* (Mm00432686_m1), *Raldh1* (Mm00657317_m1), *Il6* (Mm00446190_m1), *Vegfa* (Mm00437306_m1), *Il33* (Mm00505403_m1), and *Actb* (Mm02619580_g1). Samples were loaded in a 96-well plate (Applied Biosystems #4311971) and sealed with an Optical plate seal (Applied Biosystems #4346907) and analyzed on a StepOnePlus (Applied Biosystems).

SMART-Seq2 single-cell RNA sequencing

Briefly mice were injected with ID8 *Trp53*$^{-/-}$ (F3) or *Trp53*$^{-/-}$;*Pten*$^{-/-}$ (Pten1.14) ID8 cells and omental tumors harvested at day 28, n=4 mice per genotype. 44 macrophages per tumor were flow sorted based on DAPI$^-$ (live), CD45$^+$, CD11b$^+$, Dump$^-$ (CD3, CD19, Gr1), SiglecF$^-$, F4/80$^+$MHCII$^+$ (Table S1). SMART-Seq2 single cell library preparation was performed by the Genomics Pipelines Group (Earlham Institute) and RNA sequenced on Illumina NovaSeq 6000 SP Lane (150bp paired end) with the aim for at least 1 million reads per cell. Further details on analysis provided in **Supplementary Methods**.

CD45.1 adoptive transfer

CD45.2 mice were injected with ID8 F3 or Pten1.14 cells on day 0 (n=6 per group). Mice then received an adoptive transfer of peritoneal fluid cells either on day 1 (n=3 for both groups) or 13 days post I.P. (n=3 for F3 and n=2 for Pten1.14). A sterile peritoneal lavage (2 mM EDTA in PBS) was performed on two CD45.1 mice, samples combined and centrifuged at 330g 4 min 4°C. Cells were incubated with 5ml sterile RBC lysis buffer 5 min RT and washed in 15 ml PBS. 605,000 cells per I.P. were injected on day 1 and 400,000 cells on day 13. Omental tumors were harvested at day 28 and stained for flow cytometry.

HMOX1^{GFP} macrophage adoptive transfer

A sterile peritoneal lavage (2 mM EDTA, 0.5% FBS in PBS) was performed on healthy *Hmox1*^{GFP} mice (17) and F4/80^{hi} CD102$^+$ peritoneal macrophages were flow-sorted. 375,000 cells were adoptively transferred (AT) on

day 21 into *Hmox1*^{wt} littermates previously injected with *Trp53*$^{-/-}$;*Pten*$^{-/-}$ (Pten1.14) on day 0. Omental tumors were harvested on day 28 for flow cytometry.

Peritoneal resident macrophage ex vivo stimulation

A sterile peritoneal lavage (2 mM EDTA, 0.5% FBS in PBS) was performed on healthy female C57BL/6 mice. Lavage cells were centrifuged 330g for 5 min and pellet was resuspended in 10% FBS, 2mM Glutamine in RPMI (Sigma #R5886) and plated in a 12-well plate overnight in 20 ng/ml M-CSF (Biolegend #576404). The next day non-adherent cells were washed off and peritoneal resident macrophages were stimulated with 50 ng/ml IL33 (Biolegend #580502) for 24hr, following which RNA extraction was performed.

Analysis of single-cell RNA sequencing (scRNA-seq) data

The data from a previous scRNA-seq study of 42 high grade serous ovarian cancer patients were analysed (18) utilizing the Seurat v4.3.0 R package (19). HMOX1^{hi} macrophages were defined as macrophages that expressed *HMOX1* >1 standard deviation above the mean. The built-in FindMarkers function in the Seurat package was used to identify differentially expressed genes (DEG) and those adjusted p-values <0.05 were considered as differentially expressed. Adjusted p-values were calculated based on Bonferroni correction using all features in the dataset following Seurat manual [https://satijalab.org/seurat/v3.0/de_vignette.html]. Genes retrieved from Seurat analysis were displayed in a volcano plot using the enhancedVolcano package v1.14.0. MSigDB enrichment analysis of DEG between HMOX1^{hi} macrophages *vs* HMOX1^{lo} macrophages and between tumors with a high proportion of HMOX1^{hi} macrophages *vs* tumors with a low proportion of HMOX^{hi} macrophages was performed using msigdbr package v7.5.1 and clusterProfiler package v4.4.4 for Hallmark, Gene Ontology, and KEGG pathways.

Analysis of bulk ID8 RNA sequencing data

Bulk RNAseq data from *Trp53*$^{-/-}$;*Pten*$^{-/-}$ and *Trp53*$^{-/-}$ ID8 cells was generated as previously described (20). Briefly, raw fastq files were downloaded from GEO under accession GSE242835. These were checked for quality using FASTQC (https://www.bioinformatics.babraham.ac.uk/projects/fastqc/) and aligned to mouse genome version GRCm38 (mm10) using STAR (21). Raw counts were generated using R package Rsubread (22) and differential gene expression performed using DESeq2 (23). IPA Upstream Regulator Analysis software was used by supplying cluster 2 DEGs as input. IPA uses a z-score algorithm to make predictions which has been described in detail (24). The results were overlapped with DEGs from bulk RNAseq analysis of *Trp53*$^{-/-}$;*Pten*$^{-/-}$ and *Trp53*$^{-/-}$ ID8 cells. This naturally excluded chemicals and drugs while retaining transcription factors, cytokines, microRNAs, receptors, kinases etc.

Prognostic value of HMOX1 in an independent validation cohort

The prognostic value of *HMOX1* mRNA expression was evaluated using the Kaplan–Meier Plotter (http://kmplot.com/analysis/) (25). To analyze the overall survival (OS) of patients with HGSC (defined as ovarian cancer with serous histology and *TP53* mutation), we categorized the patients into two groups according to the best cut-off (high expression *vs.* low expression) of *HMOX1* (ID 203665_at) and assessed differences by using a Kaplan–Meier survival plot with hazard ratios, 95% confidence intervals, and log rank P values.

Statistical analyses

A p value ≤0.05 was considered statistically significant. For immunohistochemistry, statistical analyses were performed in R (v4.2.1). $HMOX1^{hi}$ expression was categorized using the optimal threshold from the maximally selected rank statistics (survminer package v0.4.9). Comparison of survival curves was performed using the logrank test. We performed COX multivariate regression of $HMOX1^{hi}$ expression on clinical parameters such as age and FIGO stage and drew forest plot for visualization using the survival package v3.5.5. All other statistical analyses were performed using Prism v.9.4.1 (GraphPad).

Data and materials availability:

Publicly available data generated by others were used by the authors - the RNA-seq data analyzed in this study were obtained from GEO at GSE242835.All data, code, and materials are available upon request. ID8 *Trp53-/-* and ID8 *Trp53-/-;Pten-/-* cells are available under materials transfer agreement (MTA) via IAMcN. Single-cell RNAseq data are available via ENA (Accession number PRJEB67876).

Results

Pten null cells are dependent on a tumor microenvironment for accelerated tumor growth.

To address how PTEN loss influences HGSC growth, we utilized matched ID8 cells with inactivating mutations in *Trp53* alone or both *Trp53* and *Pten* that we generated previously (14,15). Using multiple separate clones, we confirmed that *Trp53*$^{-/-}$;*Pten*$^{-/-}$ ID8 cells lead to significantly shortened survival compared to *Trp53*$^{-/-}$ following intraperitoneal injection (Fig. 1A). *Pten* deletion, as previously (26), did not decrease the *in vitro* doubling time in 2D high-attachment conditions (Fig. 1B, C), including those with an additional *Brca2* mutation (Fig. 1D), and under low serum and serum-starvation conditions (Fig. 1E; Fig. S1A), suggesting that enhanced intraperitoneal growth was not tumor-cell intrinsic.

Tumor cells must resist anoikis and then grow in low attachment conditions to facilitate peritoneal dissemination in HGSC. Both *Trp53*$^{-/-}$ and *Trp53*$^{-/-}$;*Pten*$^{-/-}$ ID8 clones formed spheroid-like clusters in low-attachment conditions *in vitro* (Fig. S1B), but contraction rates were equal over time in both genotypes (Fig. 1F). *In vivo*, *Pten* loss conferred no immediate survival advantage following intra-peritoneal injection (Fig. 1G; Fig. S1C). However, 14 days following injection, there was a significant expansion of *Pten* null cells in peritoneal fluid (Fig. 1G). Moreover, tumor burden in the omentum, the dominant site of metastasis in HGSC, was greater by day 14, and significantly greater by days 25-28 (Fig. 1H) in mice injected with *Trp53*$^{-/-}$;*Pten*$^{-/-}$ cells.

To ensure our findings were not ID8-specific, we utilized HGS2, a cell line generated from tumors arising in a *Trp53*$^{fl/fl}$;*Brca2*$^{fl/fl}$;*Pten*$^{fl/fl}$;*Pax8*^{Cre} transgenic mouse (16). We re-expressed Pten in HGS2 using a lentivirus (Fig. S1D, S1E), which did not impact doubling time in 2D high-attachment (Fig. 1I) or the ability to form spheroids in low-attachment (Fig. 1J, Fig. S1F) but produced smaller omental tumors *in vivo* compared to control virus-infected cells (Fig. 1K). Together, these data suggest strongly that the peritoneal microenvironment supports accelerated growth of *Pten* null tumors.

Pten null tumor cells enhance accumulation of resident-like macrophages within the omentum.

We hypothesized that macrophages support *Pten* null tumor seeding and growth. Two dominant macrophage populations exist in the peritoneal cavity and omentum in mice; F4/80^{lo}MHCII^{hi} monocyte-derived macrophages, which are constantly replenished by blood Ly6C^{hi} monocytes, and embryonically-derived F4/80^{hi}MHCII^{lo} resident macrophages, which are both self-maintained and replenished from the local F4/80^{lo}MHCII^{hi} pool (27,28). Having confirmed the specificity of our gating strategy (Fig. S2A-B), we first assessed how macrophage/monocyte populations altered during tumor growth. ID8 cell injection caused an influx of Ly6C^{hi} monocytes into peritoneal fluid within one day. This infiltration significantly increased by day 14 in *Trp53*$^{-/-}$;*Pten*$^{-/-}$-injected mice (Fig. 2A). An increase in F4/80^{lo}MHCII^{hi} macrophages, likely to derive from this monocyte pool (Fig. 2B), was also evident 14 days after *Trp53*$^{-/-}$;*Pten*$^{-/-}$ injection. The omental resident F4/80^{hi}MHCII^{lo} population increased at day 14, in *Trp53*$^{-/-}$;*Pten*$^{-/-}$-injected mice (Fig. 2C). Interestingly on day

28, when both genotypes had substantial tumor burden, *Trp53*$^{-/-}$;*Pten*$^{-/-}$ omental tumors contained significantly more resident-like macrophages across multiple subclones (Fig. 2D). Furthermore, approximately 40% of resident-like macrophages expressed the long-term residency marker TIM4^{+}, indicating that they are not newly recruited (Fig. 2E-F).

We also used *Trp53*$^{-/-}$;*Brca2*$^{-/-}$ ID8 cells with or without *Pten* deletion. Loss of *Brca2* alone did not impact resident macrophage expansion (Fig. 2G). However, the additional deletion of *Pten* again significantly increased the density of resident macrophages (Fig. 2G), which was combined with a relative paucity of monocyte-derived macrophages and T cells (Fig. 2H-I). This is coupled with an increase in *in vivo* aggressiveness (15). Deletion of *Brca2* in addition to *Pten* rescued the recruitment of monocyte-derived macrophages and T cells observed with *Pten* loss alone, (Fig. 2J-K), suggesting that *Pten* deletion alters resident macrophages specifically rather than inducing global changes in the immune microenvironment (Fig. S3A-B).

To determine if resident macrophages are drivers of *Pten* null omental tumor growth, we first depleted all macrophages using intraperitoneal clodronate-encapsulated liposomes (CEL) prior to tumor inoculation (Fig. S4A). This pan-macrophage depletion completely prevented *Trp53*$^{-/-}$;*Pten*$^{-/-}$ omental tumor formation and ascites production (Fig. 2L). Unfortunately, high mortality observed following CEL injection, as previously reported (29), precluded further studies using CEL in our institution. To dissect macrophage contribution to *Pten* null tumor growth further, we utilized mice that lack either one (*Ccr2*$^{RFP/+}$) or both copies (*Ccr2*$^{RFP/RFP}$) of *Ccr2* and consequently have markedly reduced bone marrow monocyte egress. Monocytes and monocyte-derived macrophages were significantly reduced in the peritoneal fluid and omentum in both *Ccr2*$^{RFP/+}$ and *Ccr2*$^{RFP/RFP}$ mice as expected, with no alteration in the resident macrophage pool (Fig. S4B-E) or consistent alterations in other populations (Fig. S4F-J). Strikingly, deletion of *Ccr2* significantly increased tumor burden and ascites volume in *Trp53*$^{-/-}$;*Pten*$^{-/-}$-injected mice (Fig. 2M), indicating that the monocyte-derived macrophages have a protective anti-tumoral role during *Pten* null tumor seeding and growth.

Pten null tumors drive appearance of a unique HMOX1^{hi} macrophage subpopulation.

Macrophage phenotypes cannot be simplified to binary M1/M2 marker expression and multiple distinct subtypes exist in omental tumors (30,31). Thus, we performed single-cell RNA sequencing on flow-sorted macrophages from omental tumors using the SMART-Seq2 protocol (32) (Fig. S5A). UMAP clustering revealed five distinct clusters (Fig. 3A-B). Cluster 0 expressed genes classically found in monocyte-derived macrophages, including MHCII-associated molecules (*H2-Eb1*, *H2-DMb2*, *H2-DMb1*, *H2-Ab1*, *Cd74*, *H2-Oa*, *H2-Aa*), chemokine receptors *Ccr2*, *Cx3cr1* and costimulatory molecule *Cd86* (Table S2). Cluster 0 also localized in the F4/80^{lo}MHCII^{hi} region by flow cytometry (Fig. 3C). Clusters 1 and 3 both expressed genes defined in peritoneal macrophages. Cluster 1 expressed *Fcna* (Ficolin 1), *Fn1* (Fibronectin 1) and the retinoid X receptor *Rxra* (Table S2) and was predominantly located in the F4/80^{lo}MHCII^{hi} region by flow cytometry (Fig. 3C). Cluster 3

expressed many more canonical peritoneal resident genes, including *Ltbp1*, *Garnl3*, *Serpinb2*, *Alox15*, *Selp*, *F5*, *Timd4*, *Icam2* (CD102) and *Gata6* (Table S2). Cluster 3 localized in the F4/80^{hi}MHCII^{lo} region by flow cytometry (Fig. 3C), which, taken together with the expression of TIM4 (*Timd4*), suggests that cluster 1 is a monocyte-derived precursor that transitions into cluster 3. Cluster 4 expressed genes normally found in epithelial or mesothelial cells (*Krt18*, *Krt19*, *Msln*, *Wt1*), which suggests they may be phagocytic macrophages (Table S2).

The most interesting cluster was Cluster 2, which was found almost exclusively in *Trp53*$^{-/-}$;*Pten*$^{-/-}$ tumors (Fig. 3A-B) and had high expression of Heme oxygenase 1 (*Hmox1)*, an enzyme that catalyzes the breakdown of heme into carbon monoxide, iron (Fe^{2+}) and biliverdin. Cluster 2 also expressed genes involved in lipid accumulation, such as *Trib3* (Tribbles pseudokinase-3) and *Lgals3 (*Galectin 3), as well as genes that protect against heavy metal toxicity, such as metallothioneins *Mt1* and *Mt2 (*Table S2). Cluster 2 also expressed genes associated with immunosuppression, including *Cd274 (*PD-L1), *Arg1* (Arginase 1) and *Vegfa* (Table S2). Cluster 2 localized mainly in the F4/80^{hi}MHCII^{lo} region by flow cytometry, suggesting that it may derive from resident peritoneal macrophages (Fig. 3C and Fig. S5B). We performed pseudotime analysis using Monocle3 (33) to estimate the putative direction of differentiation. When re-clustered (Fig. S5B) with cluster 0 selected as starting node, pseudotime predicted that Cluster 2 derived from Clusters 1 and 3 (Fig. 3D), indicating that it represents a subtype of peritoneal resident macrophage.

We confirmed the presence of these macrophage subpopulations by flow cytometry at early (proceeding ascites formation) and late (ascites present) time points (Fig. 3E, F and Fig. S5C, D, E). This confirmed that Cluster 2 macrophages (defined as either Arginase1^{+}PDL1^{+} or HMOX1^{hi}) were present early in *Trp53*$^{-/-}$;*Pten*$^{-/-}$ tumors and increased significantly in late tumors (Fig. 3G-H and Fig. S5C-D). We also validated the presence of HMOX1^{+} cells in ID8 omental tumor sections using immunohistochemistry (Fig. 3I), where they were observed surrounding adipocytes and in tumor borders (Fig. 3J).

We next assessed the selectivity of HMOX1 expression in Cluster 2. Using *Hmox1*^{GFP} transgenic mice (34), we confirmed that only monocytes and macrophages express HMOX1 (Fig. 3K). Although the LYVE1^{+} mesothelial lining population, which represent a small proportion of total macrophages, had the highest expression, Cluster 2 (Arginase1^{+}PDL1^{+}) highly expressed HMOX1, followed by CD102^{+} peritoneal macrophages. CD11c^{+}MHCII^{hi} monocyte-derived macrophages and monocytes had weak expression and other populations had weak/no expression. When combined, our data show that Arginase1^{+}PDL1^{+}HMOX1^{hi} macrophages are significantly enriched in *Trp53*$^{-/-}$;*Pten*$^{-/-}$ tumors (Fig. 3L).

HMOX1^{hi} macrophages derive from resident peritoneal fluid macrophages.

To test the hypothesis that peritoneal fluid resident macrophages were the prime source of HMOX1^{hi} macrophages, we first adoptively transferred CD45.1^{+} peritoneal fluid cells (which will include monocytes,

monocyte-derived and resident macrophages) into CD45.2$^+$ mice 24 hr or 13 days following ID8 cell injection. CD45.1$^+$ cells were detected in omental tumors, proving that trafficking can occur between peritoneal fluid and tumor (Fig. 4A). Interestingly resident CD45.1$^+$F4/80^{hi}MHCII^{lo} cells were enriched in *Trp53*$^{-/-}$;*Pten*$^{-/-}$ tumors (Fig. 4B-C, left panel), and correspondingly depleted in ascites (Fig. 4B-C, middle panel). The majority of CD45.1$^+$ macrophages were TIM4$^+$, indicating long-term residency (Fig. 4B-C, right panel). To determine further if HMOX1^{hi} macrophages can derive from peritoneal fluid, we sorted peritoneal fluid F4/80^{hi}CD102$^+$ cells from healthy HMOX1^{GFP} mice and adoptively transferred them into HMOX1^{wt} littermates bearing *Trp53*$^{-/-}$;*Pten*$^{-/-}$ tumors (Fig. 4D). We detected HMOX1^{GFP} cells in *Trp53*$^{-/-}$;*Pten*$^{-/-}$ omental tumors (Fig. 4E), which phenotypically copied the host's own population (CD11c$^-$MHCII^{lo}, CD102$^+$Arginase1$^+$) and almost exclusively came from long-term resident CD102$^+$TIM4$^+$ cells (Fig. 4F). However, a fraction of CD102$^-$ cells in the host macrophage pool had both high Arginase1 and PDL1 expression (Fig. 4G-H), suggesting that some Cluster 2 macrophages may also derive from non-CD102$^+$ peritoneal fluid cells.

HMOX1 inhibition extends survival.

To understand if HMOX1 is a potential therapeutic target in HGSC, we used the HMOX1-inhibitor tin mesoporphyrin (SnMP) (35). SnMP treatment did not impact the omental density of MHCII^{hi}CD11c$^+$ monocyte-derived, or CD102$^+$F4/80^{hi} macrophages (Fig. 5A-B) but did increase the density of Arginase1$^+$PDL1$^+$HMOX1$^+$ macrophages (Fig. 5C). This is likely to be a compensatory mechanism in response to HMOX1 inhibition, as SnMP is known to stimulate HMOX1 upregulation whilst still blocking enzyme activity (36). Interestingly, HMOX1 inhibition depleted LYVE1$^+$ macrophages (Fig. 5D), which suggests they are susceptible to heme-induced toxicity, in line with their proximity to tumor vasculature (37). SnMP treatment for 14 days reduced ascites formation, albeit non-significantly (p=0.078) (Fig. 5E). However, extended SnMP, given on a 5 days on/2 days off regime, significantly increased survival of *Trp53*$^{-/-}$;*Pten*$^{-/-}$ tumor-bearing mice (Hazard ratio 0.32, 95%CI 0.11–0.94, p=0.002) (Fig. 5F).

IL33 as a potential driver of Cluster 2 macrophages

To identify how *Pten* null tumor cells drive resident macrophage expansion, we initially screened chemokine and cytokine expression. This identified significantly increased *Ccl2* and *Ccl7* expression in some *Pten* null cells (Fig. S6A-C) but not in cells additionally lacking *Brca2* (Fig. S6B, C). We also analyzed the expression of retinoic acid producing enzymes *Raldh1*, *2* and *3* as peritoneal and omental resident macrophages are supported by retinoic acid, which drives their resident gene expression program, including *Gata6*. However, *Raldh1* expression was not consistently altered by *Pten* deletion (Fig. S6D), whilst *Raldh2* and *3* expression was negligible in all cells. Furthermore, *Trp53*$^{-/-}$;*Pten*$^{-/-}$ cells did not demonstrate an enhanced ability to recruit bone marrow-derived macrophages (BMDM) (Fig. S6E), whilst deletion of *Ccr2* caused a reduction in BMDM recruitment to both genotypes (Fig. S6F). *PTEN* deletion can drive IL6 production in prostate cancer (38). However, *Il6* expression was weak in *Trp53*$^{-/-}$;*Pten*$^{-/-}$ ID8 cells (C_T values 34–37) with no statistical difference

between clones (Fig. S6G) whilst IL-6 protein was undetectable by ELISA (data not shown). *Vegfa*, encoding vascular endothelial growth factor (VEGF), was also unaltered by *Pten* loss (Fig. S6H). Taken together, these data suggested that one or more factors beyond Ccl2 and Ccl7 are produced *in vivo* that support resident macrophage recruitment and expansion. The gene signature of Cluster 2 allowed us to dissect out potential drivers of HMOX1^{hi} macrophages further. We first analyzed bulk RNA sequencing analysis of *Trp53*$^{-/-}$;*Pten*$^{-/-}$ ID8 cells (20). Using this approach, we found 4505 genes significantly upregulated in *Trp53*$^{-/-}$;*Pten*$^{-/-}$ compared to *Trp53*$^{-/-}$ ID8 cells (Fig. 5G). Using Ingenuity Pathway Analysis (IPA) (Fig. 5H), we identified 25 potential upstream regulators of Cluster 2, of which 16 overlapped with genes also upregulated in *Pten* null cells (Fig. 5I). Among these genes, we identified *Il33* as a likely candidate to stimulate Cluster 2 gene expression, as it is both a secreted factor and predicted to activate one of the largest groups of genes in Cluster 2 (Fig. 5J). We confirmed increased *Il33* gene and IL-33 protein expression in *Pten* null ID8 lines (Fig. 5K). We then cultured peritoneal fluid resident macrophages in the presence of IL-33 and observed significantly increased *Hmox1* gene expression (Fig. 5L).

Mouse and human HMOX1^{hi} macrophages share common characteristics.

To ensure our murine data were relevant to HGSC patients, we analyzed a large single-cell RNA sequencing dataset, which contained data from 160 biopsies from 42 newly diagnosed, treatment naïve HGSC patients (18). Tumor-associated macrophages (n=166,895) were annotated based on known marker genes including *PTPRC*, *CD14*, *FCER1G* and *CD68*. We first categorized human macrophages based on HMOX1 expression, defining those with a scaled HMOX1 expression >1 standard deviation above the mean as HMOX1^{hi} (Fig. 6A). We then compared differentially expressed genes (DEG) in HMOX1^{hi} macrophages with those for each mouse cluster. Cluster 2 showed the highest number of overlapping genes (n=39) with those in HMOX1^{hi} cells (Fig. 6B). Similarly, of the 87 DEG in HMOX1^{hi} macrophages, the highest proportion (44.8%, n=39/87) was shared with Cluster 2 (Fig. S7A). HMOX1^{hi} macrophages were enriched in key signature genes for resident macrophages (*LYVE1*), heme metabolism (*BLVRB*), cellular response to hypoxia (*HILPDA*), metallothioneins (*MT1E*, *MT1F*, *MT1G*, *MT1H*, *MT1M*), iron transporter, storage, and homeostasis (*SLC40A1*, *HAMP*, *FTH1*, *FTL*) and lipid metabolism and storage (*APOC1*, *PLIN2*, *LIPA*) (Fig. 6C, and Table S3). Conversely, HMOX1^{lo} macrophages were enriched in interferon gamma response genes (*CXCL9*, *CXCL10*), immune cell and T cell recruitment genes (*CCL5*, *CXCL9*, *CXCL10*, *CXCL11*, *IL1B*) and MHCII gene (*HLA-DQA1*) (Fig. 6C, and Table S3). MSigDB (39) enrichment analysis of HMOX1^{hi} macrophage transcriptomes revealed an enrichment of hypoxia response, ion homeostasis, lipid metabolism and mTORC1 signaling pathways that were also found in mouse Cluster 2 (Fig. 6D, and Fig. S7B-C). Thus, human HGSC contains a cluster of macrophages that share common characteristics with mouse Cluster 2 and are characterized by high HMOX1 expression, tissue residency, oxidative stress response and low expression of pro-inflammatory cytokines/chemokines.

HMOX1^{hi} macrophages associate with poor overall survival and PI3K signaling pathway activation in HGSC

In mice, Cluster 2 macrophages were found almost exclusively in *Pten* null tumors (Fig. 3A-B). In the single-cell RNA sequencing dataset, cancer cells from tumors enriched in HMOX1^{hi} macrophages (Fig. S8A) exhibited high mTOR signaling and high insulin-like growth factor signaling (Fig. 7A), which can activate PI3K/AKT signaling (40). By contrast, immune-related pathways were downregulated in tumors enriched in HMOX1^{hi} macrophages (Fig. 7A).

Immunohistochemistry on diagnostic HGSC samples from 172 patients in the BriTROC-1 study (41) demonstrated a strong correlation between HMOX1 and CD68 (Fig. 7B-C), allowing us to use high HMOX1 expression as a surrogate for HMOX1^{hi} macrophages. The presence of HMOX1^{hi} macrophages positively correlated, albeit weakly, with positive *p*-AKT (S473) staining in tumor cells (Fig. 7D-E, Fig. S8B) and was also independently associated with reduced survival in BriTROC-1 patients, after adjustment for age and stage (HR = 1.80 [1.07-3.0]; Fig. 7F-G). The prognostic impact of high HMOX1 expression was confirmed in a separate validation cohort at the mRNA level (Fig. S8C).

Discussion

PTEN loss and other PI3K signaling alterations are frequent in HGSC but have proven challenging to target therapeutically. In this study, we have used mouse models and human HGSC samples to demonstrate that PI3K signaling pathway activation is associated with poor survival and the presence of $HMOX1^{hi}$ macrophages. Importantly, we have shown that targeting this population with a specific HMOX1 inhibitor, SnMP, extends survival in mice. This suggests that targeting deleterious tumor-infiltrating macrophages has therapeutic potential.

Macrophages are abundant in HGSC (42) but they have thus far eluded therapeutic targeting. Multiple macrophage subtypes with diverse functions exist in HGSC (18,30,31), and resident macrophages, derived from embryonic precursors, dominate the pro-tumoral response (30,31). Conversely, we show here that monocyte-derived macrophages are protective against tumor growth in *Pten* null HGSC. This corroborates previous data in which anti-CSF1R treatment following carboplatin was shown to shorten survival via inhibition of the adaptive immune response (43), and also the demonstration that stromal macrophage infiltration (44) and a high intratumoral HLA-DR:CD163 ratio correlate with improved survival (45). Collectively, this indicates strongly that macrophage therapeutic approaches need to be subtype specific.

Trans-celomic spread is the main mechanism by which HGSC disseminates around the peritoneal cavity and macrophages appear critical for this spread: gene expression in omental resident macrophages changes within hours of tumor cell injection in mice, whilst macrophages promote seeding of ID8 cells on the omentum, and macrophage depletion prior to tumor implantation prevents tumor seeding (46). This early seeding is independent of T, B and NK cells, and occurs equally well in immunodeficient models (47). Omental fat-associated lymphoid clusters (FALCs) are macrophage-rich, and resident embryonic-derived $TIM4^{+}CD163^{+}$ macrophages promote ID8 seeding and spread (30). Additionally, omental-independent mesenteric-derived resident macrophages also support dissemination (31).

PTEN loss and *PIK3CA* copy number alterations occur in HGSC carcinogenesis (48) whilst *Pten* deletion is essential for metastatic spread from the fallopian tube in transgenic murine models (49) and also accelerates intraperitoneal tumor growth (15). We show here that *Pten* deletion does not enhance proliferation or survival in low attachment conditions *per se*. However, *Pten* null cells specifically induce expansion of resident macrophages in the peritoneal fluid and omentum. Peritoneal resident macrophages support tumor spheroid formation and spread (50) and targeting them can reduce tumor burden (51). We show that *Pten* null tumors recruit peritoneal resident macrophages directly into the omentum, and that this is independent of blood monocyte recruitment, as $Ccr2^{RFP/RFP}$ and $Ccr2^{+/+}$ mice have equivalent omental resident macrophage numbers. This is important for considering targeting approaches, as recruitment does not occur directly from the blood. Furthermore, we show that *Pten* deletion accelerates formation of a unique resident macrophage population that

expresses high levels of the heme-degrading enzyme, HMOX1. We find that *Pten* null cells significantly upregulate known activators of the HMOX1^{hi} macrophage gene program, including the cytokine IL33, which is critical in inducing HMOX1 expression in red pulp macrophages (52), and drives immunosuppressive macrophage accumulation in glioblastoma (53).

HMOX1 expression is normally restricted to splenic and hepatic macrophages that remove senescent red blood cells, where its induction is cytoprotective against the oxidative stress induced by heme accumulation. However, aberrant expression in tumor associated macrophages drives immunosuppression (54), and HMOX1 inhibition by SnMP improves T cell infiltration and activity when administered with chemotherapy (54). HMOX1 also induces expression of pro-inflammatory and angiogenic genes (55), whilst HMOX1^{hi} macrophages can also directly drive metastasis, but not primary tumor growth, partly by aiding transendothelial migration and angiogenesis (56,57).

Crucially, we found that HMOX1 inhibition extended the survival of *Trp53*$^{-/-}$;*Pten*$^{-/-}$ ID8 tumor-bearing mice. SnMP is not directly cytotoxic to either tumor cells or macrophages (54) and thus SnMP anti-tumoral activity is likely to be driven only via altered macrophage function. We found high HMOX1 expression in LYVE1^{+} macrophages (34), previously shown to be mesenteric-membrane resident macrophages that can also promote ovarian cancer spread (31). We did not detect this population in our single-cell RNAseq, most likely due to the small number of cells analyzed. However, SnMP treatment did ablate LYVE1^{+} macrophages, whilst also driving an apparent increase in Cluster 2 macrophages. This reduction in LYVE1^{+} macrophages could result from their location in the perivascular niche and consequent susceptibility to heme-induced cytotoxicity (37). This suggests that the more abundant Cluster 2 macrophages may upregulate HMOX1 in part by heme, but also by other microenvironmental factors, such as, but not limited to, IL-33. Future work will be required to determine whether the LYVE1^{+} population contributes in any way to the therapeutic effect here.

There are limitations to our study, not least that most of our findings derived from the ID8 murine model of HGSC, which is of ovarian surface epithelium origin. However, ID8, and other OSE-derived models, such as STOSE (58), can recapitulate the dominant features of HGSC, namely peritoneal dissemination and omental metastasis. However, it has been shown that different murine models represent the HGSC tumor microenvironment differently, as recently demonstrated (20). For this reason, we attempted to replicate our findings using the fallopian-derived HGS2 line (16). However, we could not stably restore wild-type *Pten* in HGS2 cells using CRISPR/Cas9 due to the *Brca2* deletion and consequent defective homology-directed repair (16). Nevertheless, restoring Pten via lentivirus transduction in HGS2 cells reduced omental tumor growth. This was not consistent across all clones tested, potentially due to promoter silencing, which is known to occur in lentivirus-derived genes (59). Most importantly and reassuringly, two independent HGSC datasets validated our

findings in mice: both the scRNAseq and IHC results reinforce the finding that the presence of HMOX1^{hi} macrophages is associated with poor outcome and activated PI3K signaling in HGSC.

Correlating murine and human data is extremely challenging. Here we used *Pten* deletion to activate PI3K signaling in ID8 cells, whilst in HGSC, the pathway can be activated through multiple additional mechanisms, including *PIK3CA* and *AKT* mutation and amplification. We used *p*-AKT staining on IHC as a surrogate for pathway activation in patient samples, but it remains unclear whether every mechanism for activating PI3K signaling will generate HMOX1^{hi} macrophages. Similarly, the number of scRNAseq datasets available to interrogate tumor specific PI3K signaling remains small, and further data will be necessary to elucidate more nuanced biomarkers of pathway activity.

In summary, we have shown that HMOX1^{hi} macrophages, with common gene expression programs including immunosuppression, hypoxia, cholesterol efflux, and lipid transport, can be identified in both murine and human HGSC. The function of HMOX1^{hi} macrophages in HGSC remains to be understood fully and the gene expression pathways may reflect both PI3K-driven microenvironment that induces HMOX1^{hi} cells and overall macrophage function. Nonetheless, our study highlights that HMOX1 inhibition may provide a relevant treatment strategy for HGSC.

Acknowledgments

We thank the Imperial College London Central Biomedical Services for their expertise, advice, and assistance in performing all *in vivo* experiments. We also thank Dr Keira Turner for help performing *in vivo* experiments. We also thank Dr William Jackson for expertise and helpful discussion over results. We thank both the LMS/NIHR Imperial Biomedical Research Centre Flow Cytometry Facility and Department of Natural Sciences Flow Facility, Imperial College London for their help FACS-sorting and performing flow cytometry experiments. We thank Ignazio Puccio and Hiromi Kudo and the Section of Pathology, Department of Metabolism, Digestion and Reproduction, Imperial College London for the preparation of tissues for histology and IHC staining. We thank Dr Iain Macaulay and the Genomics Pipelines Group, Earlham Institute for their expertise and performing the SMART-Seq2 single cell sequencing. We thank Dr Nina Moderau, Department of Surgery and Cancer, Imperial College London for advice and access to reagents to perform lentivirus experiments.

We are very grateful to all patients and their families that have provided samples that made this scientific research possible.

Funding:

This work was funded by Ovarian Cancer Action (references P72914, P76567 and PSF687) and Cancer Research UK (grant reference C608/A15973). JNA is supported by grants from Cancer Research UK (DCRPGF\100009) and Cancer Research Institute / Wade F.B. Thompson CLIP grant (CRI3645). Infrastructure support was provided by the NIHR Imperial Biomedical Research Centre and the Imperial Experimental Cancer Medicine Centre, but this was not used to support mouse experiments. IMcN also receives funding as an NIHR Senior Investigator. OLS is a recipient of grants from La Ligue contre le Cancer, La Fondation Nuovo-Soldati, and Canceropole Lyon Auvergne Rhone-Alpes. The funders had no role in study design, data collection and analysis, decision to publish or preparation of the manuscript. YX is funded by a joint PhD scholarship between Imperial College London and China Scholarship Council (201808060050). NI is funded by Imperial College London President's PhD Scholarship. JW was funded by a CRUK PhD studentship.

Author contributions:

Conceptualization: SS, IAMcN

Methodology: SS, OLS, HBM, JNA, JBW, IAMcN

Investigation: SS, OLS, HBM, KT, FGF, CW, SJ, DPE, NI, CAH, YX, PS, DPC, ET

Visualization: SS, OLS, HBM, IAMcN

Resources: JDB

Supervision: HCK, JNA, APC-P, BCV, IAMcN,

Writing—original draft: SS, IAMcN

Writing—review & editing: All authors

References

1. Ray-Coquard I, Pautier P, Pignata S, Perol D, Gonzalez-Martin A, Berger R, *et al.* Olaparib plus Bevacizumab as First-Line Maintenance in Ovarian Cancer. N Engl J Med **2019**;381:2416-28
2. Zhang L, Conejo-Garcia JR, Katsaros D, Gimotty PA, Massobrio M, Regnani G, *et al.* Intratumoral T cells, recurrence, and survival in epithelial ovarian cancer. N Engl J Med **2003**;348:203-13
3. Goode E, OTTA. Dose-Response Association of CD8+ Tumor-Infiltrating Lymphocytes and Survival Time in High-Grade Serous Ovarian Cancer. JAMA Oncol **2017**;3:e173290
4. TCGA. Integrated genomic analyses of ovarian carcinoma. Nature **2011**;474:609-15
5. Sato E, Olson SH, Ahn J, Bundy B, Nishikawa H, Qian F, *et al.* Intraepithelial CD8+ tumor-infiltrating lymphocytes and a high CD8+/regulatory T cell ratio are associated with favorable prognosis in ovarian cancer. Proc Natl Acad Sci U S A **2005**;102:18538-43
6. Matulonis UA, Shapira-Frommer R, Santin AD, Lisyanskaya AS, Pignata S, Vergote I, *et al.* Antitumor Activity and Safety of Pembrolizumab in Patients with Advanced Recurrent Ovarian Cancer: Results from the Phase 2 KEYNOTE-100 Study. Annals of Oncology **2019**;30:1080-87
7. Deniger DC, Pasetto A, Robbins PF, Gartner JJ, Prickett TD, Paria BC, *et al.* T-cell responses to TP53 "hotspot" mutations and unique neoantigens expressed by human ovarian cancers. Clin Cancer Res **2018**;24:5562-73
8. Alexandrov LB, Nik-Zainal S, Wedge DC, Aparicio SA, Behjati S, Biankin AV, *et al.* Signatures of mutational processes in human cancer. Nature **2013**;500:415-21
9. Patch A-M, Christie EL, Etemadmoghadam D, Garsed DW, George J, Fereday S, *et al.* Whole–genome characterization of chemoresistant ovarian cancer. Nature **2015**;521:489-94
10. Zhang X, Wang A, Han L, Liang B, Allard G, Diver E, *et al.* PTEN Deficiency in Tubo-Ovarian High-Grade Serous Carcinoma is Associated with Poor Progression-Free Survival and is Mutually Exclusive with CCNE1 Amplification. Mod Pathol **2023**;36:100106
11. Martins FC, Santiago I, Trinh A, Xian J, Guo A, Sayal K, *et al.* Combined image and genomic analysis of high-grade serous ovarian cancer reveals PTEN loss as a common driver event and prognostic classifier. Genome biology **2014**;15:526
12. Hanrahan AJ, Schultz N, Westfal ML, Sakr RA, Giri DD, Scarperi S, *et al.* Genomic complexity and AKT dependence in serous ovarian cancer. Cancer Discov **2012**;2:56-67
13. Banerjee S, Giannone G, Clamp AR, Ennis DP, Glasspool RM, Herbertson R, *et al.* Efficacy and Safety of Weekly Paclitaxel Plus Vistusertib vs Paclitaxel Alone in Patients With Platinum-Resistant Ovarian High-Grade Serous Carcinoma: The OCTOPUS Multicenter, Phase 2, Randomized Clinical Trial. JAMA Oncology **2023**;9:675-82
14. Walton JB, Blagih J, Ennis D, Leung E, Dowson S, Farquharson M, *et al.* CRISPR/Cas9-mediated Trp53 and Brca2 knockout to generate improved murine models of ovarian high grade serous carcinoma. Cancer Res **2016**;76:6118-29
15. Walton JB, Farquharson M, Mason S, Port J, Kruspig B, Dowson S, *et al.* CRISPR/Cas9-derived models of ovarian high grade serous carcinoma targeting Brca1, Pten and Nf1, and correlation with platinum sensitivity. Scientific reports **2017**;7:16827
16. Maniati E, Berlato C, Gopinathan G, Heath O, Kotantaki P, Lakhani A, *et al.* Mouse Ovarian Cancer Models Recapitulate the Human Tumor Microenvironment and Patient Response to Treatment. Cell reports **2020**;30:525-40.e7
17. Anstee JE, Opzoomer JW, Dean I, Muller HP, Bahri M, Liakath-Ali K, *et al.* Perivascular macrophages collaborate to facilitate chemotherapy resistance in cancer. bioRxiv **2022**:2022.02.03.478952
18. Vázquez-García I, Uhlitz F, Ceglia N, Lim JLP, Wu M, Mohibullah N, *et al.* Ovarian cancer mutational processes drive site-specific immune evasion. Nature **2022**;612:778-86
19. Butler A, Hoffman P, Smibert P, Papalexi E, Satija R. Integrating single-cell transcriptomic data across different conditions, technologies, and species. Nature biotechnology **2018**;36:411-20
20. Cook DP, Galpin KJC, Rodriguez GM, Shakfa N, Wilson-Sanchez J, Echaibi M, *et al.* Comparative analysis of syngeneic mouse models of high-grade serous ovarian cancer. Commun Biol **2023**;6:1152
21. Dobin A, Davis CA, Schlesinger F, Drenkow J, Zaleski C, Jha S, *et al.* STAR: ultrafast universal RNA-seq aligner. Bioinformatics (Oxford, England) **2013**;29:15-21

22. Liao Y, Smyth GK, Shi W. The R package Rsubread is easier, faster, cheaper and better for alignment and quantification of RNA sequencing reads. Nucleic Acids Res **2019**;47:e47
23. Love MI, Huber W, Anders S. Moderated estimation of fold change and dispersion for RNA-seq data with DESeq2. Genome biology **2014**;15:550
24. Krämer A, Green J, Pollard J, Jr., Tugendreich S. Causal analysis approaches in Ingenuity Pathway Analysis. Bioinformatics (Oxford, England) **2014**;30:523-30
25. Szász AM, Lánczky A, Nagy Á, Förster S, Hark K, Green JE, *et al.* Cross-validation of survival associated biomarkers in gastric cancer using transcriptomic data of 1,065 patients. Oncotarget **2016**;7:49322-33
26. Nikolatou K, Sandilands E, Román-Fernández A, Cumming EM, Freckmann E, Lilla S, *et al.* PTEN deficiency exposes a requirement for an ARF GTPase module for integrin-dependent invasion in ovarian cancer. The EMBO Journal **2023**:e113987
27. Bain CC, Gibson DA, Steers NJ, Boufea K, Louwe PA, Doherty C, *et al.* Rate of replenishment and microenvironment contribute to the sexually dimorphic phenotype and function of peritoneal macrophages. Science immunology **2020**;5
28. Ghosn EE, Cassado AA, Govoni GR, Fukuhara T, Yang Y, Monack DM, *et al.* Two physically, functionally, and developmentally distinct peritoneal macrophage subsets. Proc Natl Acad Sci U S A **2010**;107:2568-73
29. Li Z, Xu X, Feng X, Murphy PM. The Macrophage-depleting Agent Clodronate Promotes Durable Hematopoietic Chimerism and Donor-specific Skin Allograft Tolerance in Mice. Scientific reports **2016**;6:22143
30. Etzerodt A, Moulin M, Doktor TK, Delfini M, Mossadegh-Keller N, Bajenoff M, *et al.* Tissue-resident macrophages in omentum promote metastatic spread of ovarian cancer. J Exp Med **2020**;217:e20191869
31. Zhang N, Kim SH, Gainullina A, Erlich EC, Onufer EJ, Kim J, *et al.* LYVE1+ macrophages of murine peritoneal mesothelium promote omentum-independent ovarian tumor growth. J Exp Med **2021**;218:e20210924
32. Picelli S, Faridani OR, Björklund AK, Winberg G, Sagasser S, Sandberg R. Full-length RNA-seq from single cells using Smart-seq2. Nature protocols **2014**;9:171-81
33. Trapnell C, Cacchiarelli D, Grimsby J, Pokharel P, Li S, Morse M, *et al.* The dynamics and regulators of cell fate decisions are revealed by pseudotemporal ordering of single cells. Nature biotechnology **2014**;32:381-6
34. Anstee JE, Feehan KT, Opzoomer JW, Dean I, Muller HP, Bahri M, *et al.* LYVE-1(+) macrophages form a collaborative CCR5-dependent perivascular niche that influences chemotherapy responses in murine breast cancer. Developmental cell **2023**;58:1548-61.e10
35. Wong RJ, Vreman HJ, Schulz S, Kalish FS, Pierce NW, Stevenson DK. In vitro inhibition of heme oxygenase isoenzymes by metalloporphyrins. J Perinatol **2011**;31 Suppl 1:S35-41
36. Marinissen MJ, Tanos T, Bolós M, de Sagarra MR, Coso OA, Cuadrado A. Inhibition of heme oxygenase-1 interferes with the transforming activity of the Kaposi sarcoma herpesvirus-encoded G protein-coupled receptor. J Biol Chem **2006**;281:11332-46
37. Opzoomer JW, Anstee JE, Dean I, Hill EJ, Bouybayoune I, Caron J, *et al.* Macrophages orchestrate the expansion of a proangiogenic perivascular niche during cancer progression. Science advances **2021**;7:eabg9518
38. Zhao D, Cai L, Lu X, Liang X, Li J, Chen P, *et al.* Chromatin Regulator CHD1 Remodels the Immunosuppressive Tumor Microenvironment in PTEN-Deficient Prostate Cancer. Cancer Discov **2020**;10:1374-87
39. Liberzon A, Birger C, Thorvaldsdóttir H, Ghandi M, Mesirov JP, Tamayo P. The Molecular Signatures Database (MSigDB) hallmark gene set collection. Cell systems **2015**;1:417-25
40. Lau MT, Leung PC. The PI3K/Akt/mTOR signaling pathway mediates insulin-like growth factor 1-induced E-cadherin down-regulation and cell proliferation in ovarian cancer cells. Cancer Lett **2012**;326:191-8
41. Smith P, Bradley T, Gavarró LM, Goranova T, Ennis DP, Mirza HB, *et al.* The copy number and mutational landscape of recurrent ovarian high-grade serous carcinoma. Nat Commun **2023**;14:4387

42. Pearce OMT, Delaine-Smith R, Maniati E, Nichols S, Wang J, Bohm S, *et al.* Deconstruction of a metastatic tumor microenvironment reveals a common matrix response in human cancers. Cancer Discov **2018**;8:304-19
43. Heath O, Berlato C, Maniati E, Lakhani A, Pegrum C, Kotantaki P, *et al.* Chemotherapy induces tumor-associated macrophages that aid adaptive immune responses in ovarian cancer. Cancer immunology research **2021**;9:665-81
44. Montfort A, Owen S, Piskorz AM, Supernat A, Moore L, Al-Khalidi S, *et al.* Combining measures of immune infiltration shows additive effect on survival prediction in high-grade serous ovarian carcinoma. Br J Cancer **2020**
45. Zhang M, He Y, Sun X, Li Q, Wang W, Zhao A, *et al.* A high M1/M2 ratio of tumor-associated macrophages is associated with extended survival in ovarian cancer patients. Journal of ovarian research **2014**;7:19
46. Krishnan V, Tallapragada S, Schaar B, Kamat K, Chanana AM, Zhang Y, *et al.* Omental macrophages secrete chemokine ligands that promote ovarian cancer colonization of the omentum via CCR1. Commun Biol **2020**;3:524
47. Clark R, Krishnan V, Schoof M, Rodriguez I, Theriault B, Chekmareva M, *et al.* Milky spots promote ovarian cancer metastatic colonization of peritoneal adipose in experimental models. Am J Pathol **2013**;183:576-91
48. Cheng Z, Mirza H, Ennis DP, Smith P, Morrill Gavarró L, Sokota C, *et al.* The Genomic Landscape of Early-Stage Ovarian High-Grade Serous Carcinoma. Clin Cancer Res **2022**;28:2911-22
49. Perets R, Wyant GA, Muto KW, Bijron JG, Poole BB, Chin KT, *et al.* Transformation of the fallopian tube secretory epithelium leads to high-grade serous ovarian cancer in brca;tp53;pten models. Cancer Cell **2013**;24:751-65
50. Yin M, Li X, Tan S, Zhou HJ, Ji W, Bellone S, *et al.* Tumor-associated macrophages drive spheroid formation during early transcoelomic metastasis of ovarian cancer. J Clin Invest **2016**;126:4157-73
51. Casanova-Acebes M, Menendez-Gutierrez MP, Porcuna J, Alvarez-Errico D, Lavin Y, Garcia A, *et al.* RXRs control serous macrophage neonatal expansion and identity and contribute to ovarian cancer progression. Nat Commun **2020**;11:1655
52. Lu H, Cunnea P, Nixon K, Rinne N, Aboagye EO, Fotopoulou C. Discovery of a biomarker candidate for surgical stratification in high-grade serous ovarian cancer. Br J Cancer **2021**;124:1286-93
53. De Boeck A, Ahn BY, D'Mello C, Lun X, Menon SV, Alshehri MM, *et al.* Glioma-derived IL-33 orchestrates an inflammatory brain tumor microenvironment that accelerates glioma progression. Nat Commun **2020**;11:4997
54. Muliaditan T, Opzoomer JW, Caron J, Okesola M, Kosti P, Lall S, *et al.* Repurposing Tin Mesoporphyrin as an Immune Checkpoint Inhibitor Shows Therapeutic Efficacy in Preclinical Models of Cancer. Clin Cancer Res **2018**;24:1617-28
55. Alaluf E, Vokaer B, Detavernier A, Azouz A, Splittgerber M, Carrette A, *et al.* Heme oxygenase-1 orchestrates the immunosuppressive program of tumor-associated macrophages. JCI insight **2020**;5
56. Consonni FM, Bleve A, Totaro MG, Storto M, Kunderfranco P, Termanini A, *et al.* Heme catabolism by tumor-associated macrophages controls metastasis formation. Nature immunology **2021**;22:595-606
57. Muliaditan T, Caron J, Okesola M, Opzoomer JW, Kosti P, Georgouli M, *et al.* Macrophages are exploited from an innate wound healing response to facilitate cancer metastasis. Nat Commun **2018**;9:2951
58. McCloskey CW, Goldberg RL, Carter LE, Gamwell LF, Al-Hujaily EM, Collins O, *et al.* A new spontaneously transformed syngeneic model of high-grade serous ovarian cancer with a tumor-initiating cell population. Frontiers in oncology **2014**;4:53
59. Herbst F, Ball CR, Tuorto F, Nowrouzi A, Wang W, Zavidij O, *et al.* Extensive methylation of promoter sequences silences lentiviral transgene expression during stem cell differentiation in vivo. Mol Ther **2012**;20:1014-21

Figures and Tables

Figure 1: *Pten* null cells are dependent on a tumor microenvironment for accelerated tumor growth.

A) Survival curve for mice injected with ID8 *Trp53*$^{-/-}$ (clones F3, M20 and C7), and *Trp53*$^{-/-}$;*Pten*$^{-/-}$ (clones Pten1.12, Pten1.14, and Pten1.15), n=6 per clone. Statistical significance was tested using the Log-rank (Mantel-Cox) test.

B) ID8 *Trp53*$^{-/-}$ (F3) and *Trp53*$^{-/-}$;*Pten*$^{-/-}$ (Pten1.14) cells grown in flat high-attachment plates were imaged every 4hr over 72 hr. Each data point represents the average of 3-4 technical replicates per clone and 4 images per replicate. Data were generated as phase object count per well normalized to first scan ("0 hr"). Representative data from experiment shown.

C) Mean doubling time of ID8 cells grown in **B)** conditions for 72hr. Each data point represents a clone grown at a different passage or different clone; an average of 3-4 wells, and 4 images per well were used to generate each data point. Clones plated as follows *Trp53*$^{-/-}$ ID8-F3 (circle), ID8-M20 (square), and *Trp53*$^{-/-}$;*Pten*$^{-/-}$, ID8-F3; Pten1.14 (circle), ID8-F3;Pten1.15 (triangle). Significance was tested by an unpaired t-test.

D) Mean doubling time of ID8 subclones grown in 2D under same conditions as in **C)**, clones used were *Trp53*$^{-/-}$ (F3), *Trp53*$^{-/-}$;*Pten*$^{-/-}$ (Pten1.14), *Trp53*$^{-/-}$;*Brca2*$^{-/-}$ (Brca2 2.14) and *Trp53*$^{-/-}$;*Brca2*$^{-/-}$;*Pten*$^{-/-}$ (Brca2.14 Pten22). Statistical significance was tested using an ordinary one-way ANOVA, with Šidák's multiple comparison test on selected pairs.

E) ID8 *Trp53*$^{-/-}$ (F3), *Trp53*$^{-/-}$;*Pten*$^{-/-}$ (Pten1.14) cells were seeded and grown in 4%, 0.4% or 0% FBS for up to 72hr and the doubling time was calculated as in **C)**. Each symbol represents the average of technical triplicates, performed over 3 passages (P1, P4 and P5). Statistical significance was tested using an ordinary one-way ANOVA, with Šidák's multiple comparison test on selected pairs.

F) ID8 clones *Trp53*$^{-/-}$ (F3), *Trp53*$^{-/-}$;*Pten*$^{-/-}$ (Pten1.14) were grown in low-attachment u-bottomed plates for 168 hr. Each symbol represents the average of technical triplicates, repeated on two passages. The largest brightfield object area (μm^2) per image was quantified and shown over time.

G) Mice were injected with either PBS, *Trp53*$^{-/-}$ (F3) or *Trp53*$^{-/-}$;*Pten*$^{-/-}$ (Pten1.14) ID8 cells on day 0 and a peritoneal lavage was performed on days 1, 2, 7, and 14. The ID8 cell count was estimated by flow cytometry (gated on as CD45-, SSC-A^{hi}, Live). Each point represents an individual mouse. Statistical significance was tested using an ordinary one-way ANOVA, with Šidák's multiple comparison test on selected pairs.

H) Mice were injected with *Trp53*$^{-/-}$ (F3) or *Trp53*$^{-/-}$;*Pten*$^{-/-}$ (Pten1.14) ID8 cells on day 0 and the omental tumors harvested at days 14, 25 and 28. Tumor weights shown are pooled from a several experiments, including control groups from other studies. Each point represents an individual mouse. Triangles indicate mice received artificial sweetener in their drinking water for 14 days prior to ID8 injection. Significance was tested by an ordinary one-way ANOVA, with Šidák's multiple comparison test on selected pairs.

I) Mean doubling times of HGS2 lentivirus-transduced clones grown for 72 hr in the same conditions as in **C)**. Each circle represents average of 2 technical replicates from one passage with 9 images taken per well.

Clones E1, F6, and F8 were transduced with control GFP lentivirus, and clones C9, E11, and F3 were transduced with Pten GFP lentivirus. Significance was tested by an ordinary one-way ANOVA, with Tukey's multiple comparison test.

J) HGS2 subclones were grown in low-attachment u-bottomed plates for 90 hr. Each symbol represents the average of technical triplicates per subclone, performed at a different passage. The largest brightfield object area (μm^2) per image was quantified and shown over time.

K) HGS2 parental cells, control lentivirus or Pten lentivirus transduced subclones were injected I.P. into mice, and omental tumors harvested. Each symbol represents an individual mouse. Omental tumor weights are shown when harvested on days 56 (white) or 59 (filled). Control lentivirus clones F6 (triangle) and F8 (circle), and Pten lentivirus clones C9 (triangle), E11 (circle) and F3 (square). Significance was tested by one-way ANOVA, with Šidák's multiple comparisons test.

In all experiments, results are considered significant when $p<0.05$ and ns=not significant.

Figure 2: *Pten* null tumor cells enhance accumulation of resident-like macrophages within the omentum.

A-C) Mice were injected with either ID8 *Trp53*$^{-/-}$ (F3) or *Trp53*$^{-/-}$;*Pten*$^{-/-}$ (Pten1.14) cells. Peritoneal fluid and omenta were harvested 1, 2, 7 and 14 days later. Flow cytometry was performed for indicated cell populations. Counting beads were used to estimate absolute cell numbers, normalized to either the total lavage fluid (ml) or per omentum. Gating strategy for **A)** monocytes: Zombie Yellow$^-$, CD45$^+$, CD11b$^+$, Ly6C^{hi}. Macrophages: Zombie Yellow$^-$, CD45$^+$, CD11b$^+$, Ly6C$^-$, Ly6G$^-$, SiglecF$^-$, **B)** F4/80^{lo}, MHCII^{hi} (monocyte-derived) or **C)** F4/80^{hi}, MHCII^{lo} (resident-like). Every data point represents an individual mouse. Statistical significance was tested using a one-way ANOVA with Šidák's multiple comparison test on selected samples.

D-F) Mice were injected with individual ID8 *Trp53*$^{-/-}$ (F3, C7 and M20) or *Trp53*$^{-/-}$;*Pten*$^{-/-}$ clones (Pten1.12, Pten1.14 and Pten1.15) on day 0 and omental tumors harvested at day 28 for flow cytometry. **D)** Resident macrophages were defined as Zombie Yellow$^-$, CD45$^+$, CD11b$^+$, Ly6C$^-$, Ly6G$^-$, SiglecF$^-$, F4/80^{hi}, MHCII^{lo} and normalized to omental tumor weight (mg).

E) Representative gating strategy used to define TIM4$^+$ cells within the F4/80^{hi}MHCII^{lo} population. **F)** Quantification of percentage TIM4$^+$ cells out of total F4/80^{hi}MHCII^{lo} macrophages. Statistical significance was tested using a one-way ANOVA with Šidák's multiple comparison test on selected samples.

G) Mice were injected with ID8 *Trp53*$^{-/-}$ (F3), *Trp53*$^{-/-}$;*Pten*$^{-/-}$ (Pten1.14), *Trp53*$^{-/-}$;*Brca2*$^{-/-}$ (Brca2 2.14) or *Trp53*$^{-/-}$;*Brca2*$^{-/-}$;*Pten*$^{-/-}$ (Brca2.14 Pten22) clones and the number of resident macrophages quantified by flow cytometry as in **D)**.

H) Density of monocyte-derived, defined as Zombie Yellow$^-$, CD45$^+$, CD11b$^+$, Ly6C$^-$, Ly6G$^-$, SiglecF$^-$, F4/80^{lo}, MHCII^{hi} cells in omental tumors of same mice as in **D)**.

I) Density of T cells, defined as Zombie Yellow$^-$, CD45$^+$, CD3$^+$ in omental tumors of same mice as in **D)**.

J) Density of monocyte-derived, defined as Zombie Yellow$^-$, CD45$^+$, CD11b$^+$, Ly6C$^-$, Ly6G$^-$, SiglecF$^-$, F4/80^{lo}, MHCII^{hi} cells in omental tumors of same mice as in **G)**.

K) Density of T cells, defined as Zombie Yellow$^-$, CD45$^+$, CD3$^+$ in omental tumors of same mice as in **G)**.

L) Clodronate encapsulated liposomes (CEL) (n=6 mice) or PBS (n=3) were injected I.P. into mice on -14, -7 and -1 days prior to *Trp53*$^{-/-}$;*Pten*$^{-/-}$ (Pten1.12) tumor cell injection. CEL or PBS was then administered on days +7, +14, +21. Mice were harvested on day 26 (circles), apart from one PBS-treated mouse that reached endpoint at day 23 (triangle) and the omental tumor weight (mg) and ascites fluid volume (ml) was analyzed. Statistical significance was tested using an unpaired t-test.

M) *Ccr2*$^{+/+}$, *Ccr2*$^{RFP/+}$, *Ccr2*$^{RFP/RFP}$ (clear symbols) or in-house wild-type (filled symbols) age-matched mice were injected with either *Trp53*$^{-/-}$ (F3) or *Trp53*$^{-/-}$;*Pten*$^{-/-}$ (Pten1.14) ID8 cells on day 0 and culled on day 28. Omental tumor weight (mg) and ascites fluid volume (ml) were measured. Statistical significance was tested using a one-way ANOVA with Šidák's multiple comparison test on selected samples (omental tumors) or with Tukey's multiple comparison test (ascites).

In all experiments, results are considered significant when $p<0.05$ and ns=not significant.

Figure 3: *Pten* null tumors drive accelerated formation of unique HMOX1^{hi} macrophage subpopulation.

A) Mice were injected with ID8 *Trp53*$^{-/-}$ (F3) or *Trp53*$^{-/-}$;*Pten*$^{-/-}$ (Pten1.14) ID8 cells on day 0 and omental tumors harvested at day 28, with n=4 mice per genotype. Macrophages were single-cell flow sorted based on DAPI$^-$ (live), CD45$^+$, CD11b$^+$, Dump$^-$ (CD3, CD19, Gr1), SiglecF$^-$, F4/80$^+$MHCII$^+$, singlets and analysed by plate-based SMART-Seq2 single cell RNA sequencing. Following quality filtering, a UMAP projection of macrophages is shown, using Seurat pipeline. Selected significantly differentially expressed genes (DEGs) (defined as adjusted p value <0.05 and average log2-fold change >0) are shown next to respective cluster. Total DEGs per cluster are Cluster 0; 1022 genes, Cluster 1; 59 genes, Cluster 2; 425 genes, Cluster 3; 141 genes and Cluster 4; 1625 genes.

B) The percentage of macrophages identified in each cluster isolated from either ID8 *Trp53*$^{-/-}$ and *Trp53*$^{-/-}$;*Pten*$^{-/-}$ omental tumors from **A)** is shown.

C) The expression of F4/80 and MHCII per macrophages, as collected during index sorting is shown with cluster identity overlaid by color.

D) Data in **A)** were reanalyzed using the Monocle 3 package and Pseudotime analysis applied (shown as heatmap), with the root node placed in cluster 0.

E) Mice were injected with ID8 *Trp53*$^{-/-}$ or *Trp53*$^{-/-}$;*Pten*$^{-/-}$ ID8 cells on day 0 and omental tumors harvested at early (day 28 *Trp53*$^{-/-}$; day 21 *Trp53*$^{-/-}$;*Pten*$^{-/-}$, "E") and late (day 47 *Trp53*$^{-/-}$; day 28 *Trp53*$^{-/-}$;*Pten*$^{-/-}$, "L") timepoints. The density of macrophages in omental tumors was calculated for F4/80$^+$MHCII$^+$, CX3CR1$^+$MHCII^{hi}CD86$^+$CD11c$^+$. Statistical significance was tested by one-way ANOVA and Tukey's multiple comparison test.

F) As in **E)** the density of macrophages in omental tumors was calculated for F4/80$^+$MHCII$^+$, LYVE1$^-$ CD102$^+$TIM4$^+$. Statistical significance was tested by One-way ANOVA and Tukey's multiple comparison test.

G) As in **E)** the density of macrophages in omental tumors was calculated for F4/80^{+}MHCII^{+}, LYVE1^{-}CD102^{-} TIM4^{-}Arginase1^{+}PDL1^{+}. Statistical significance was tested by One-way ANOVA and Tukey's multiple comparison test.

H) As in **E)** The density of macrophages in omental tumors was calculated for F4/80^{+}MHCII^{+}, HMOX1^{hi}. Statistical significance was tested by One-way ANOVA and Tukey's multiple comparison test.

I) ID8 *Trp53*$^{-/-}$ (F3) or *Trp53*$^{-/-}$;*Pten*$^{-/-}$ (Pten1.14) omental tumors harvested at day 28 were stained for HMOX1 by immunohistochemistry. The number of HMOX1^{hi} cells was quantified using QuPath. Statistical significance was tested using an unpaired t-test.

J) Representative immunohistochemistry images of HMOX1 (brown stain) from *Trp53*$^{-/-}$ and *Trp53*$^{-/-}$;*Pten*$^{-/-}$ tumors from **I)** are shown, scale bar is indicated in the image.

K) HMOX1^{GFP} mice (n=2) were injected with ID8 *Trp53*$^{-/-}$;*Pten*$^{-/-}$ (Pten1.14) cells on day 0 and omental tumors harvested at day 25. Representative histogram of HMOX1-GFP expression is shown per cell population. The CD45^{-} population will contain transgenic stromal cells as well as the GFP^{-} ID8 cells.

L) Gating strategy used to define cluster 2; F4/80^{+}MHCII^{+}, LYVE1^{-}, CD11c^{-}, MHCII^{lo}, CD102^{-}, F4/80^{lo}, HMOX1^{hi}, Arginase1^{+}, PDL1^{+} (left). Density of cluster 2 macrophages in day 28 ID8 *Trp53*$^{-/-}$ (F3) or *Trp53*$^{-/-}$;*Pten*$^{-/-}$ (Pten1.14) tumors (right). Statistical significance was tested using an unpaired t-test.

In all experiments, results are considered significant when $p<0.05$ and ns=not significant.

Figure 4: HMOX1^{hi} macrophages are partially derived from resident peritoneal fluid macrophages.

A) CD45.2 mice were injected with ID8 *Trp53*$^{-/-}$ (F3) or *Trp53*$^{-/-}$;*Pten*$^{-/-}$ (Pten1.14) cells on day 0 (n=6 per group). Mice then received an adoptive transfer (AT) of CD45.1 peritoneal fluid cells on either day 1 (n=3) or day 13 (n=3 for F3 and n=2 for Pten1.14) post ID8 I.P. Tumors and ascites were harvested at day 28. One mouse was excluded as there were insufficient cells and thus became a negative control. Representative flow cytometry gating strategy for live CD45.1 and CD45.2 cells in omental tumors. An FMO-CD45.1 control and no AT control are also shown.

B) The omental tumors from **A)** were analysed by flow cytometry. The percentage resident F4/80^{hi}MHCII^{lo} macrophages of all CD45.1 cells in omental tumor (left) and ascites (middle) are shown for mice that received CD45.1 AT 24hr post ID8 injection. The percentage TIM4^{+} out of F4/80^{hi}MHCII^{lo}CD45.1^{+} macrophages in omental tumor is also shown (right). One mouse had no detectable F4/80^{hi}MHCII^{lo} macrophages, therefore the %TIM4^{+} value was not able to be analyzed. Black values are from ID8 *Trp53*$^{-/-}$ (F3)-injected mice and pink are from *Trp53*$^{-/-}$;*Pten*$^{-/-}$ (Pten1.14)-injected mice. Statistical significance was tested by unpaired t-test.

C) The omental tumors from **A)** were analyzed by flow cytometry. The percentage resident F4/80^{hi}MHCII^{lo} macrophages of all CD45.1 cells in the omental tumor (left) and ascites (middle) are shown for mice that received CD45.1 AT 13 days post ID8 injection. The percentage TIM4^{+} out of F4/80^{hi}MHCII^{lo}CD45.1^{+} macrophages in omental tumor is also shown (right). Black values are from ID8 *Trp53*$^{-/-}$ (F3)-injected mice

and pink are from *Trp53*$^{-/-}$;*Pten*$^{-/-}$ (Pten1.14)-injected mice. Statistical significance was tested by unpaired t-test.

D) F4/80^{hi} CD102^{+} peritoneal macrophages were FACS sorted from healthy *Hmox1*^{GFP} mice and adoptively transferred (AT) into *Hmox1*^{wt} littermates bearing ID8 *Trp53*$^{-/-}$;*Pten*$^{-/-}$ (Pten1.14) tumors on day 21. Omental tumors and ascites were harvested on day 28.

E) Representative FACS plot of GFP^{+} cells in the CD45^{+} live gated cells in an omental tumor. The relative fluorescence GFP^{+} cells (green) compared to GFP^{-} cells (grey) is shown for markers CD11b, MHCII, CD11c, CD102, Arginase1, and PDL1.

F) Macrophages were gated as previously, and the percentage of cells within each gate out of total detected GFP^{+} cells is shown.

G) The percentage of each macrophage population gated within GFP^{+} (green) or GFP^{-} (grey) cells that is positive for Arginase1.

H) The percentage of each macrophage population gated within GFP^{+} (green) or GFP^{-} (grey) cells that is positive for PDL1.

In all experiments, results are considered significant when $p<0.05$ and ns=not significant.

Figure 5: HMOX1 inhibition extends the survival in mice bearing *Pten* null ID8 tumors.

A) Mice were injected with ID8 *Trp53*$^{-/-}$ (F3) or *Trp53*$^{-/-}$;*Pten*$^{-/-}$ (Pten1.14) cells on day 0. From day 14, mice received 25 µmol/kg SnMP (n=6) or vehicle control (n=6) daily for 14 days. Omental tumors were harvested on day 28 and analysed by flow cytometry. The density of CD11c^{+}MHCII^{hi} macrophages in the omental tumors is shown. Statistical significance was tested using one-way ANOVA and with Šidák's multiple comparisons test with selected comparisons.

B) The density of CD102^{+}F4/80^{hi} macrophages from A) is shown per mg omental tumor. Statistical significance was tested using one-way ANOVA and Šidák's multiple comparisons test with selected comparisons.

C) The density of Arginase1^{+}PDL1^{+}HMOX1^{+} macrophages from A) is shown per mg omental tumor. Statistical significance was tested using one-way ANOVA and Šidák's multiple comparisons test with selected comparisons.

D) The density of LYVE1^{+} macrophages from A) is shown per mg omental tumor. Statistical significance was tested using one-way ANOVA and Tukey's multiple comparison test.

E) The ascites volume from A). Statistical significance was tested using one-way ANOVA and Šidák's multiple comparisons test with selected comparisons.

F) Mice were injected with ID8 *Trp53*$^{-/-}$;*Pten*$^{-/-}$ (Pten1.14) cells on day 0. From day 14, mice received 25 µmol/kg SnMP (n=9) or vehicle control (n=9) daily on a 5 days on/2 days off schedule until mice were harvested reached humane endpoint, which included advanced abdominal swelling. One mouse was censored in the SnMP group as it was killed before reaching endpoint at end of study (day 42); it had minimal disease present. Statistical significance was tested using a log-rank (Mantel-Cox) test.

G) Volcano plot depicting log-2 normalized fold change and FDR adjusted p-values for gene expression differences between and *Trp53*$^{-/-}$;*Pten*$^{-/-}$ and *Trp53*$^{-/-}$ ID8 cells. Cluster 2 activators are individually labelled.

H) List of Cluster 2 activators and inhibitors as identified through the IPA analysis.

I) Venn diagram showing the overlap of genes upregulated in *Trp53*$^{-/-}$;*Pten*$^{-/-}$ cells and genes which are predicted to activate cluster 2 genes identified through the IPA analysis. Among these 25 predicted activators, 16 were found common among the genes upregulated in *Trp53*$^{-/-}$;*Pten*$^{-/-}$ bulk RNAseq analysis.

J) Bicycle wheel diagram showing the 29 genes expressed by Cluster 2 macrophages which are activated or inhibited by *Il33*, identified through the IPA analysis.

K) *Il33* gene (left) and IL-33 protein expression (right) in ID8 clones. Each data point represents a clone. Clones plated as follows *Trp53*$^{-/-}$ ID8-F3 (circle), ID8-M20 (square), ID8-C7 (triangle) and *Trp53*$^{-/-}$;*Pten*$^{-/-}$, ID8-F3; Pten1.12 (square) ID8-F3; Pten1.14 (circle), ID8-F3;Pten1.15 (triangle). Significance was tested by an unpaired t-test.

L) Peritoneal fluid macrophages were cultured *in vitro* for 24hr in the presence of 50 ng/ml recombinant IL-33 protein or untreated media control. *Hmox1* gene expression was then assessed.

In all experiments, results are considered significant when $p<0.05$ and ns=not significant.

Figure 6: Mouse and human HMOX1^{hi} macrophages share common characteristics in HGSC.

A) Scaled and centered HMOX1 expression on tumor associated macrophages. Macrophages with a scaled HMOX1 expression above 1 standard deviation from the mean were defined as HMOX1^{hi}. Macrophages with a scaled HMOX1 expression below 1 standard deviation from the mean were defined as HMOX1^{lo}.

B) The overlap between DEG found in human HMOX1^{hi} macrophages and DEG found in each mouse macrophage cluster 0-4 is shown.

C) DEG in HMOX1^{hi} macrophages (right side of the volcano plot) and HMOX1^{lo} macrophages (left side) defined in **A)** from human HGSC tumors is shown.

D) Comparison of MSigDB pathway enrichment in human HMOX1^{hi} macrophages and mouse cluster 2 macrophages showing selected pathways of interest that were significantly enriched (Hallmark, Gene Ontology, KEGG).

Figure 7: A high proportion of HMOX1^{hi} macrophages is associated with poor overall survival and PI3K signaling pathway activation.

A) MSigDB enrichment analysis (Hallmark, Gene Ontology, KEGG) of HGSC tumors with high *vs* low proportion of HMOX1^{hi} macrophages showing selected pathways of interest that were significantly enriched (left) or downregulated (right). Pathways relating to PI3K-signalling are highlighted in red.

B) CD68 (top left) and HMOX1 (top right) immunohistochemistry staining in the BriTROC-1 study TMA. QuPath positive cell detection is shown (in red) for CD68 (bottom left) and HMOX1 (bottom right). Scale bar represents 200 μm.

C) Spearman correlation between the proportion of HMOX1^{hi} macrophages and the proportion of CD68^{+} macrophages found in BriTROC-1 TMA cores.

D) *p*-AKT staining in the BriTROC-1 study with (left) and without (right) the QuPath tumor classifier showing weak (1+), moderate (2+) and strong (3+) staining.

E) Spearman correlation between *p*-AKT tumor H-score and the average proportion of HMOX1^{hi} macrophages per patient in the BriTROC-1 study.

F) Overall survival of patients in the BriTROC-1 study with high (n=76) and low (n=50) proportion of HMOX1^{hi}, where the cut-off is based on the optimal threshold. Statistical comparison was performed using the logrank test.

G) Multivariate regression forest plot of HMOX1^{hi} expression.

Figure 1

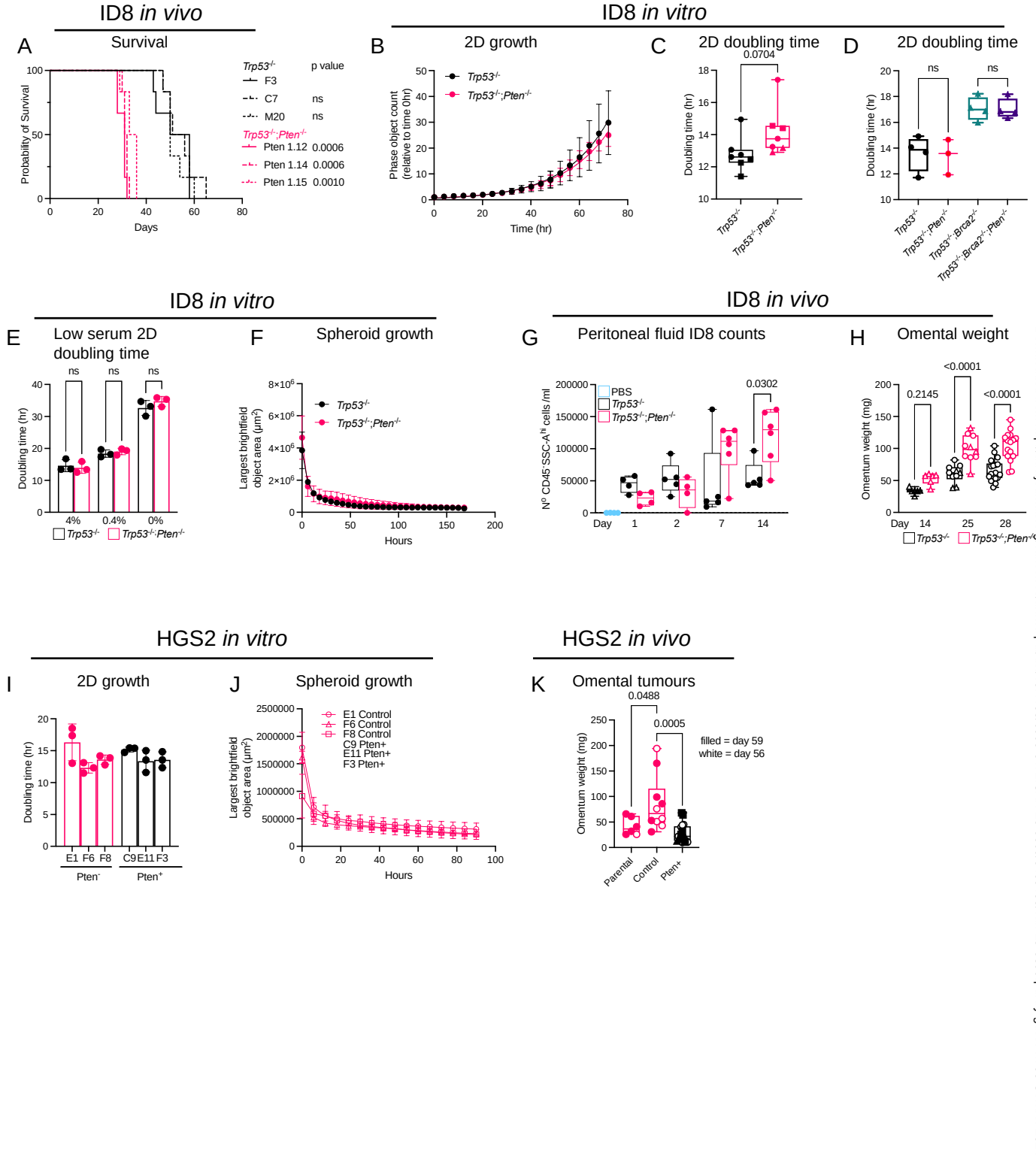

Figure 2

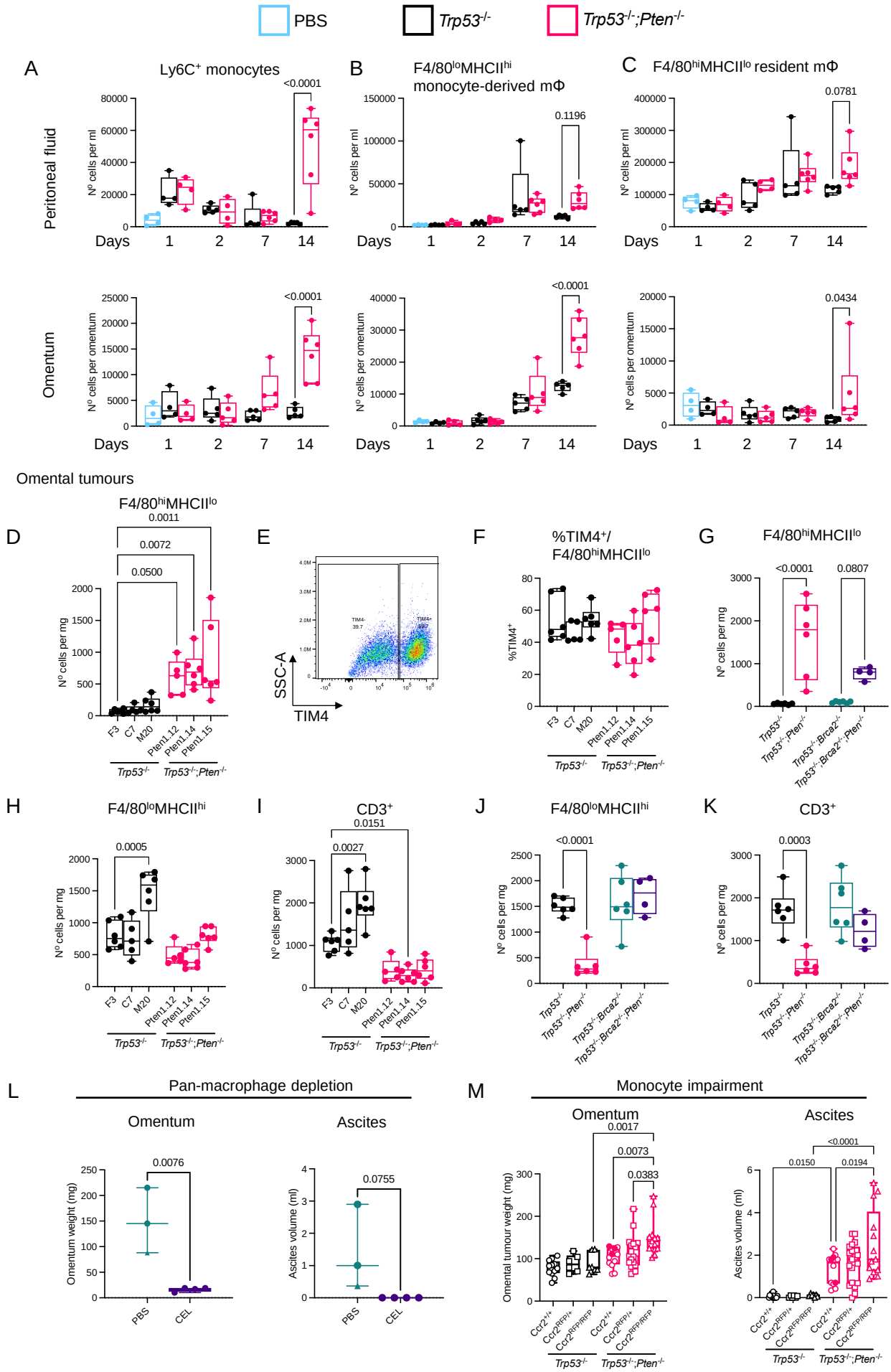

Figure 3

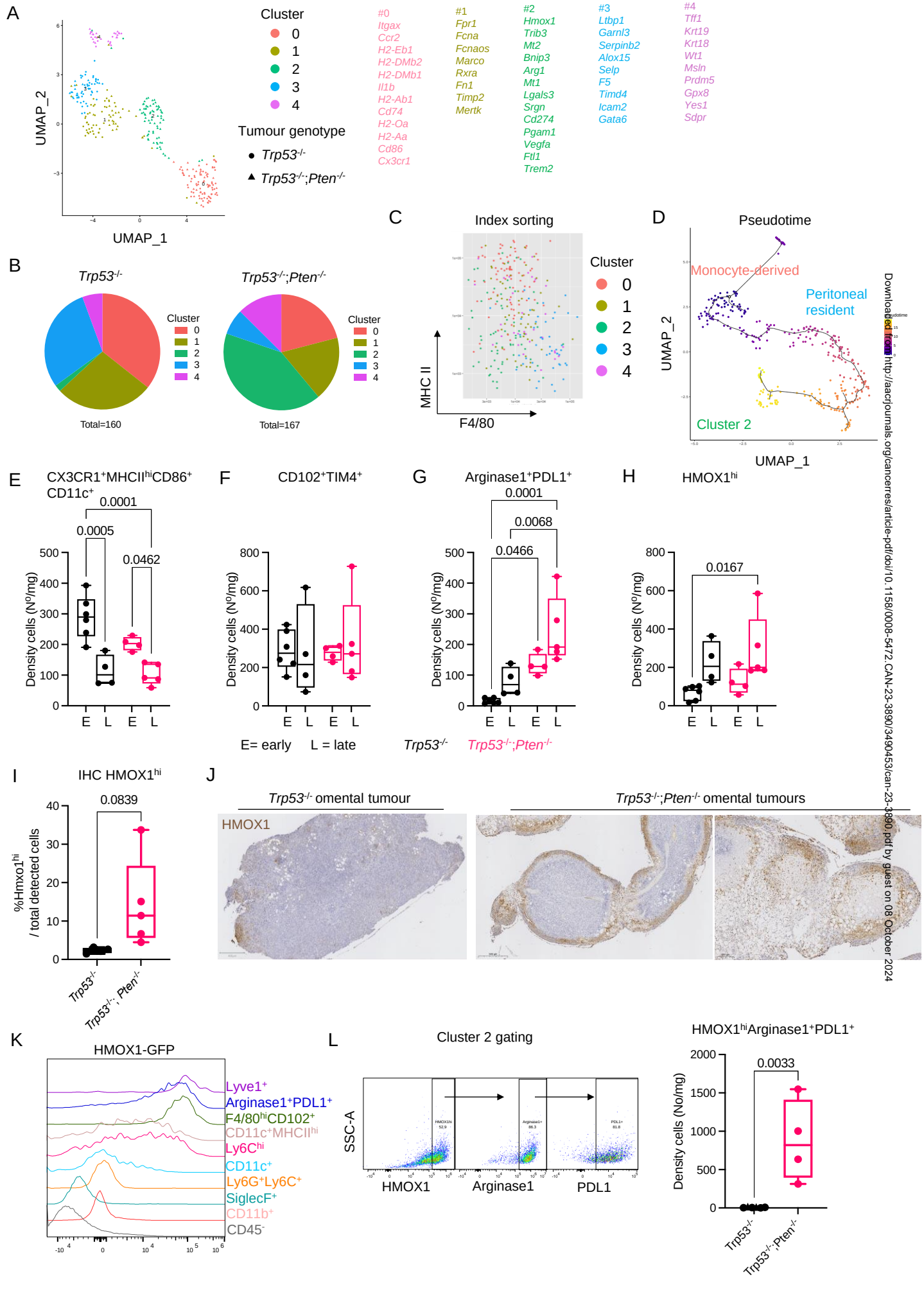

Figure 4

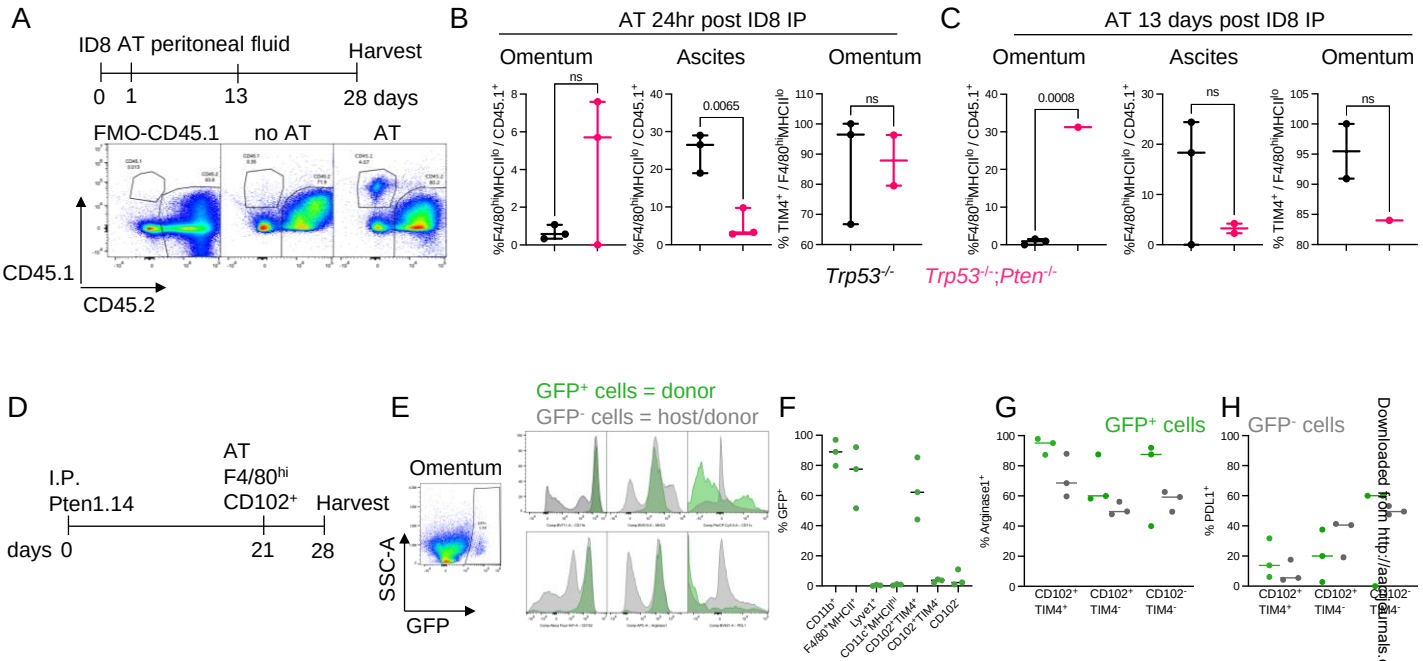

Figure 5

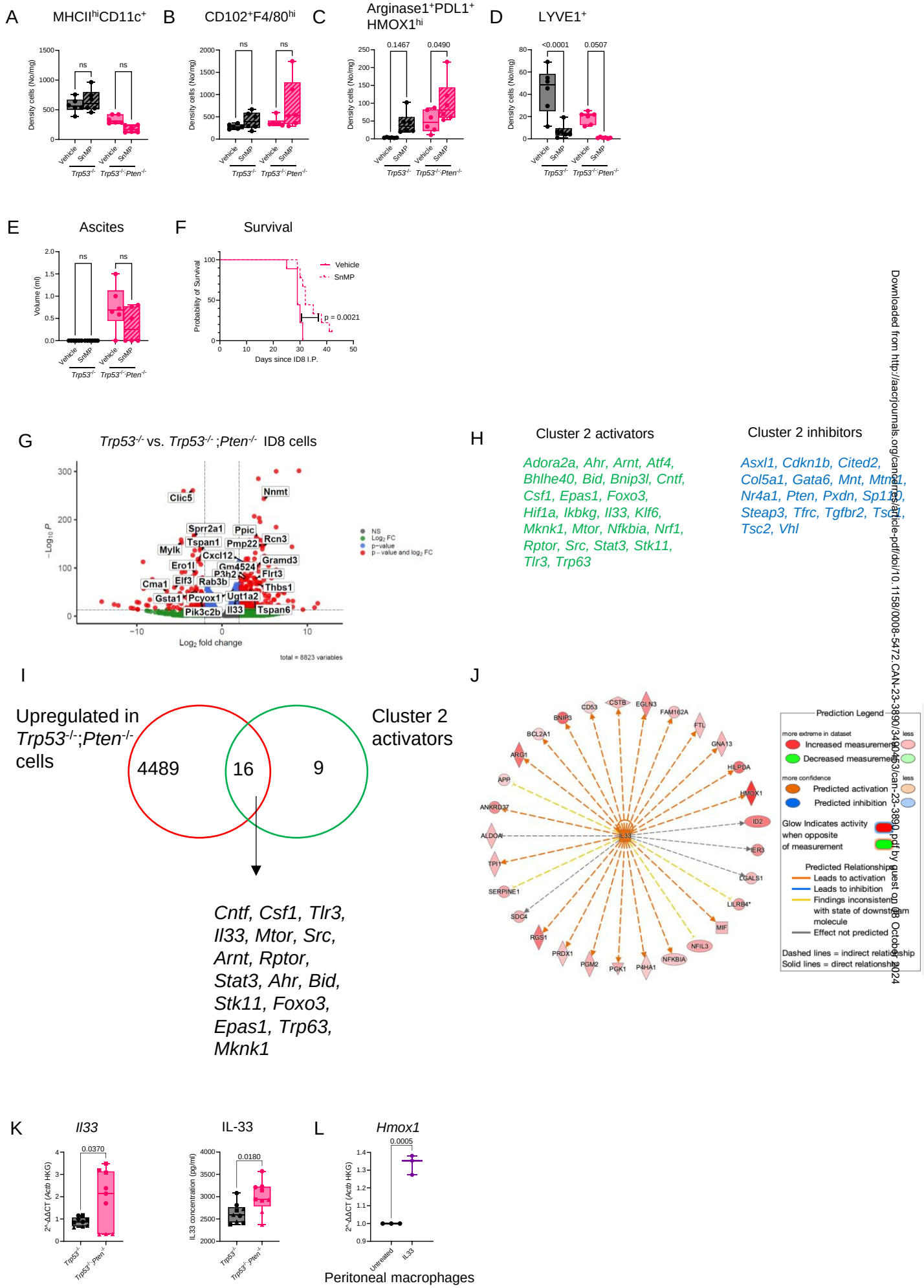

Figure 6

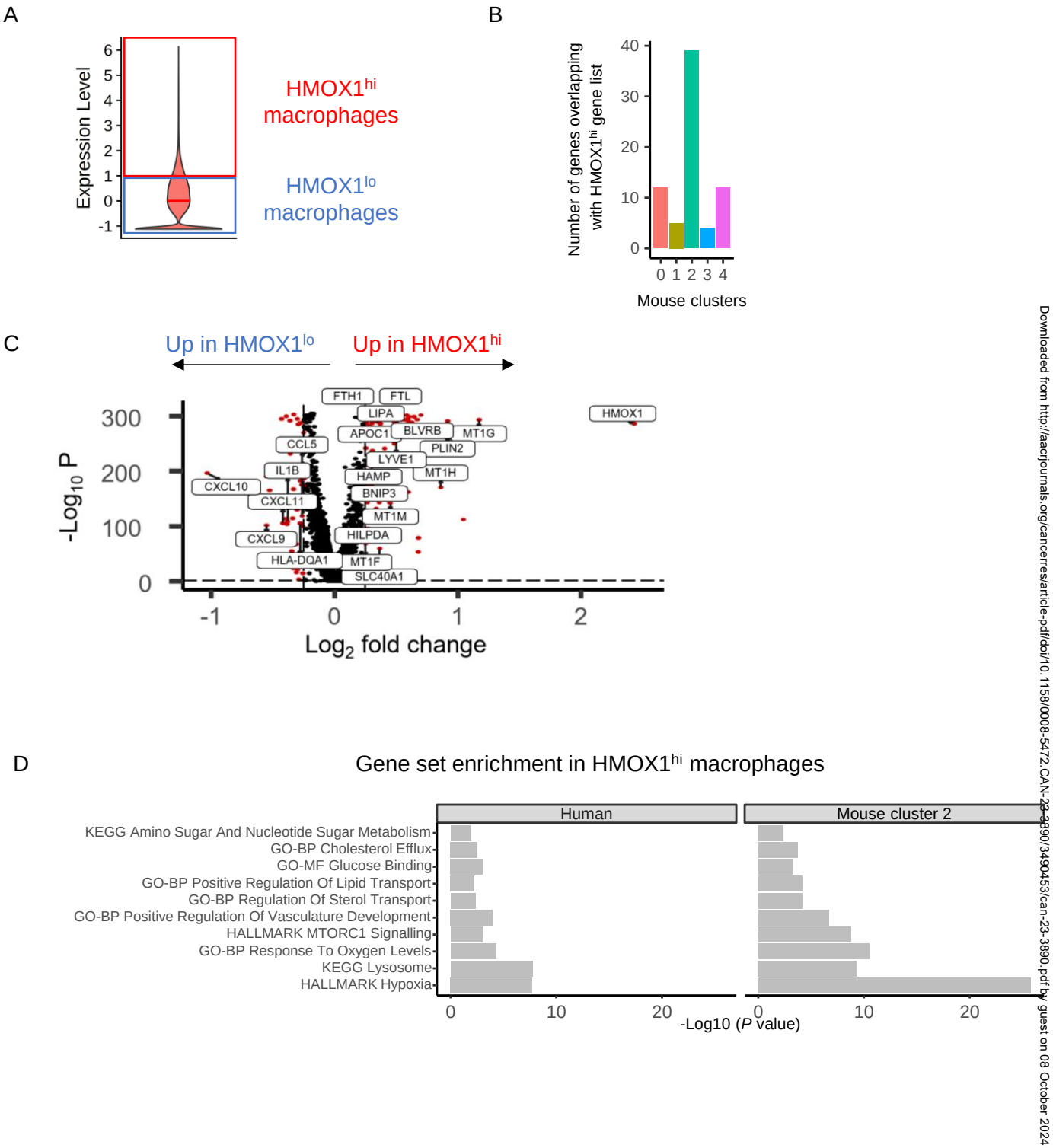

Figure 7